

# Handing-Off the Outcome of Binary Neutron Star Mergers for Accurate and Long-Term Post-Merger Simulations

Federico G. Lopez Armengol,<sup>1</sup> Zachariah B. Etienne,<sup>2,3,4</sup> Scott C. Noble,<sup>5</sup> Bernard J. Kelly,<sup>6,5,7</sup> Leonardo R. Werneck,<sup>2,3,4</sup> Brendan Drachler,<sup>1,8</sup> Manuela Campanelli,<sup>1,9,8</sup> Federico Cipolletta,<sup>1,10</sup> Yosef Zlochower,<sup>1,9,8</sup> Ariadna Murguia-Berthier,<sup>11,12,13</sup> Lorenzo Ennoggi,<sup>1</sup> Mark Avara,<sup>1</sup> Riccardo Ciolfi,<sup>14,15</sup> Joshua Faber,<sup>1,9,8</sup> Grace Fiacco,<sup>1,8,16</sup> Bruno Giacomazzo,<sup>17,18,19</sup> Tanmayee Gupte,<sup>1,8</sup> Trung Ha,<sup>1,20</sup> Julian H. Krolik,<sup>21</sup> Vassilios Mewes,<sup>22</sup> Richard O'Shaughnessy,<sup>1,9,8</sup> Jesús M. Rueda-Becerril,<sup>1</sup> and Jeremy Schnittman<sup>5</sup>

<sup>1</sup>*Center for Computational Relativity and Gravitation,  
Rochester Institute of Technology, Rochester, New York 14623, USA*

<sup>2</sup>*Department of Physics, University of Idaho, Moscow, ID 83843, USA*

<sup>3</sup>*Department of Physics and Astronomy, West Virginia University, Morgantown, WV 26506*

<sup>4</sup>*Center for Gravitational Waves and Cosmology, West Virginia University,  
Chestnut Ridge Research Building, Morgantown, WV 26505*

<sup>5</sup>*Gravitational Astrophysics Lab, NASA Goddard Space Flight Center, Greenbelt, MD 20771, USA*

<sup>6</sup>*Department of Physics, University of Maryland Baltimore County, 1000 Hilltop Circle Baltimore, MD 21250, USA*

<sup>7</sup>*Center for Research and Exploration in Space Science and Technology,  
NASA Goddard Space Flight Center, Greenbelt, MD 20771, USA*

<sup>8</sup>*School of Physics and Astronomy, Rochester Institute of Technology, Rochester, New York 14623, USA*

<sup>9</sup>*School of Mathematical Sciences, Rochester Institute of Technology, Rochester, New York 14623, USA*

<sup>10</sup>*Leonardo Corporate LABS - via Raffaele Pieragostini 80, 16149 Genova GE - Italy*

<sup>11</sup>*Department of Astronomy and Astrophysics, University of California, Santa Cruz, CA 95064, USA*

<sup>12</sup>*Center for Interdisciplinary Exploration and Research in Astrophysics  
(CIERA), 1800 Sherman Ave., Evanston, IL 60201, USA*

<sup>13</sup>*NASA Einstein Fellow*

<sup>14</sup>*INAF, Osservatorio Astronomico di Padova, Vicoletto dell'Osservatorio 5, I-35122 Padova, Italy*

<sup>15</sup>*INFN, Sezione di Padova, Via Francesco Marzolo 8, I-35131 Padova, Italy*

<sup>16</sup>*Department of Physics, Montana State University, Bozeman, Montana 59717, USA*

<sup>17</sup>*Università degli Studi di Milano - Bicocca, Dipartimento di Fisica G. Occhialini, Piazza della Scienza 3, I-20126 Milano, Italy*

<sup>18</sup>*INFN, Sezione di Milano-Bicocca, Piazza della Scienza 3, I-20126 Milano, Italy*

<sup>19</sup>*INAF, Osservatorio Astronomico di Brera, via E. Bianchi 46, I-23807 Merate (LC), Italy*

<sup>20</sup>*Department of Physics, University of North Texas, Denton, Texas 76203, USA*

<sup>21</sup>*Physics and Astronomy Department, Johns Hopkins University, Baltimore, MD 21218, USA*

<sup>22</sup>*National Center for Computational Sciences, Oak Ridge National Laboratory,  
P.O. Box 2008, Oak Ridge, TN 37831-6164, USA*

(Dated: December 21, 2021)

We perform binary neutron star (BNS) merger simulations in full dynamical general relativity with ILLINOISGRMHD, on a Cartesian grid with adaptive-mesh refinement. After the remnant black hole (BH) has become nearly stationary, the evolution of the surrounding accretion disk on Cartesian grids over long timescales ( $\sim 1$ s) is suboptimal, as the plasma flows obliquely across coordinate lines and numerical errors quickly dissipate angular momentum from the disk. To address this, we present the HANDOFF, a set of computational tools that enables the transfer of general relativistic magnetohydrodynamic (GRMHD) and spacetime data from ILLINOISGRMHD to HARM3D, a GRMHD code that specializes in modeling BH accretion disks in static spacetimes over long timescales, making use of general coordinate systems with spherical topology. We demonstrate that the HANDOFF allows for a smooth and reliable transition of GRMHD fields and spacetime data, enabling us to efficiently and reliably evolve BNS dynamics well beyond merger. We also discuss future plans, which involve incorporating advanced equations of state and neutrino physics into BNS simulations using the HANDOFF approach.

## I. INTRODUCTION

The detection of the gravitational wave (GW) GW170817 and its electromagnetic counterparts confirms long-standing theses about the outcomes of binary neutron star (BNS) mergers. Although this event remains unique, the current high rate of GW detections suggests that similar events will follow [1]. The signal GW170817 is compatible with a BNS merger of total mass  $\sim 2.73 M_{\odot}$

and mass ratio  $0.73 - 1.0$  (low spins assumed), in the galaxy NGC 4993 [2] at a distance of  $\sim 40$  Mpc [3, 4].

The observation of the coincident short  $\gamma$ -ray burst (SGRB) GRB 170817A after  $1.7$ s from the merger [5] supports earlier theoretical connections between SGRB and BNS mergers [6–10]. In the standard picture, the merger remnant powers a mildly relativistic jet that drills through the post-merger medium and generates a hot cocoon. The jet-cocoon system eventually breaks out from the dense ejecta and releases  $\gamma$ -rays over wide angles

[11–14].

Kilonova emission detected in UV-optical-IR bands within the first hours and weeks after merger is consistent with radioactive heating from neutron-rich elements synthesized in the ejecta that decay either via  $\beta$ -decay,  $\alpha$ -decay, or spontaneous fission [15–20]. This proves that BNS mergers are a propitious environment for the rapid neutron-capture process (r-process) and play an important role in the nucleosynthesis of the universe [21–25]. More specifically, an early “blue” component in the kilonova spectrum, and a later “red” component, reveal multi-component ejecta, the former being lanthanide-poor, with lower opacity, plausibly ejected from the polar region of the remnant, and the latter being lanthanide-rich, with higher opacity, and tidally ejected around the equator of the system [see, for instance, Ref. 26].

Moreover, later light-curves in radio [27] and X-rays [28] rise together in time as  $\sim t^{0.8}$  [29], consistent with a single power-law of index  $-0.6$  for synchrotron radiation, emitted by accelerated electrons in the shocked interstellar medium (ISM) [30]. The quick decline of these light-curves as  $\sim t^{-2.2}$  after their peaks at 150 days after merger [31, 32], and the measurement of apparent superluminal motion with very long-baseline interferometry (VLBI) [33] proves that this outflow is powered by an anisotropic and mildly-relativistic outflow, viewed off-axis by  $15^\circ - 30^\circ$ , consistent with the picture of the jet-cocoon break-out [see also Refs. 34, 35].

Although this physical model is in agreement with the available data, many questions remain unanswered [see the reviews 36–40]. The equation of state (EoS) for the neutron stars (NSs) has been constrained by the GW signal and EM counterparts [4, 41], but remains degenerate [see 42, and references therein]. While the remnant compact object seems to have collapsed to a black hole (BH), the time of collapse remains uncertain, and the central engine for the jet could be both a rotating BH or a *long-lived* hyper-massive neutron star (HMNS) [see 43–45]. Furthermore, the dependence of the total mass, composition, and magnetization of the ejecta on the properties of the binary, remains to be fully understood [see 46, 47].

Numerical simulations are key to answering these questions but, despite the remarkable progress in the last decades [48–74], there are still computational limitations to address. The key ingredients for a realistic simulation of a BNS merger and post-merger are, at least, *Numerical Relativity* (NR) for the evolution of the spacetime metric during the inspiral and merger, *General-Relativistic Magnetohydrodynamics* (GRMHD) for the evolution of the matter fields, realistic EoS as tabulated from nuclear interactions, and consistent emission, absorption and transport of neutrinos [see the reviews 36, 37, 74]. However, numerical codes that take NR into account usually make use of Cartesian coordinates in a hierarchy of inset boxes with different resolutions (Adaptive Mesh Refinement, AMR) and adopt a finest resolution of  $\sim 200$  m [75]. Such a grid topology and resolution are insufficient

to resolve in detail the length-scales of the relevant mechanisms of the post-merger, like the magneto-rotational instability [MRI; see Ref. 76]. Moreover, the outer boundary of such domains is usually at  $\sim 5000$  km, preventing long-term simulations ( $\sim 1$  s) that can follow the propagation of the outflows [see Refs. 46, 77]. See Ref. [44] for further comments on current computational limitations, and see Ref. [78] for NR simulations in spherical coordinates.

In this work we solve these computational problems by transitioning a BNS post-merger simulation from the code ILLINOISGRMHD [79] that uses Cartesian AMR grids, to the code HARM3D [80, 81] that adopts a grid adapted to the requirements of the post-merger. HARM3D’s grid uses spherical-like coordinates for better conservation of angular momentum; the grid has higher resolution in the polar coordinate towards the equator if close to the BH, to resolve the disk, but higher resolution towards the polar axis if farther away, to resolve the jet-cocoon system. Further its outer boundary is far enough ( $\sim 10^5$  km) to include the region of the jet-breakout. Finally, we use novel boundary conditions at the polar axis that allow us to fully resolve the funnel region. Transitioning between ILLINOISGRMHD and HARM3D is possible because they rest on the same formalism for describing the GRMHD fields. However the numerical infrastructures of these codes are very different. Our new code HANOFF consists of the set of routines needed to translate the state of a BNS post-merger from ILLINOISGRMHD to HARM3D, and the description and validation of this package entails the main purpose of this work.

Our work is organized as follows. In Sec. II we describe the formalism and numerical methods adopted by the numerical codes ILLINOISGRMHD and HARM3D, and we describe in detail the set of routines that compose the HANOFF. In Sec. III we validate the HANOFF in the well-known system of a magnetized torus around a rotating BH. Then in Sec. IV we apply the HANOFF to a BNS post-merger, and show the continued evolution in HARM3D gives the results expected. Finally, in Sec. V we present final remarks and our future work.

## II. THE HANOFF PACKAGE

We first describe the GRMHD formalism adopted by both ILLINOISGRMHD and HARM3D, as well as the steps performed by the HANOFF package that allow us to transition a BNS post-merger simulation from one code to the other. In Fig. 1 we show a sketch of the workflow around the HANOFF: We perform a BNS merger simulation until BH formation with ILLINOISGRMHD. At the same time, we design and export the numerical grid that we will use to continue the post-merger evolution in HARM3D. We interpolate the MHD primitives and spacetime metric of the post-merger onto this grid, and use these results to construct restart files readable by HARM3D. Then we select results from lower or higher

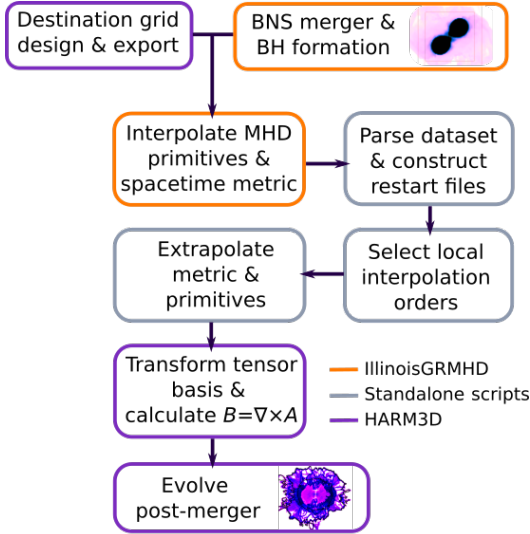


FIG. 1. HANDOFF package workflow. The colors of the borders shows the code responsible for the task, with *orange* for ILLINOISGRMHD, *grey* for standalone scripts, and *purple* for HARM3D.

orders of interpolation, depending on the local smoothness of each grid function. If the destination grid is larger than the original grid of ILLINOISGRMHD, we extrapolate the primitives and spacetime metric to populate the complementary cells. Finally, we transform the tensor basis from Cartesian coordinates to the new coordinate system, calculate the magnetic field from the curl of the magnetic vector potential, and continue the post-merger evolution in the new grid with the usual methods of HARM3D.

### A. GRMHD Formalism

The GRMHD formalisms on which ILLINOISGRMHD and HARM3D are based are equivalent, but the formulation and conventions adopted by each code differ. Below we present the equations of motion as implemented in HARM3D, and we will describe the differences with ILLINOISGRMHD when presenting the methods adopted for the BNS merger.

The evolution of the MHD fields follows from the integration of the general relativistic equations of motion for a perfect fluid with infinite conductivity (ideal MHD). These are the continuity equation, the local conservation of energy and momentum, and Maxwell's equations [see, for instance, Refs. 79–82]. In flux-conservative form, they read:

$$\partial_t \mathbf{U}(\mathbf{P}) = -\partial_i \mathbf{F}^i + \mathbf{S}(\mathbf{P}), \quad (1)$$

where  $\mathbf{P}$  is the vector of *primitive* variables,  $\mathbf{U}$  the vector

of *conserved* variables,  $\mathbf{F}$  the *fluxes*, and  $\mathbf{S}$  the *sources*:

$$\mathbf{P} = [\rho, p, \tilde{v}^k, B^k]^T, \quad (2)$$

$$\mathbf{U}(\mathbf{P}) = \sqrt{-g} [\rho u^t, T^t{}_t + \rho u^t, T^t{}_j, B^k]^T, \quad (3)$$

$$\mathbf{F}^i(\mathbf{P}) = \sqrt{-g} [\rho u^i, T^i{}_t + \rho u^i, T^i{}_j, (b^i u^k - b^k u^i)]^T, \quad (4)$$

$$\mathbf{S}(\mathbf{P}) = \sqrt{-g} [0, T^\kappa{}_\lambda \Gamma^\lambda{}_{t\kappa}, T^\kappa{}_\lambda \Gamma^\lambda{}_{j\kappa}, 0^k]^T, \quad (5)$$

where  $g$  denotes the determinant of the metric,  $\rho$  is the rest mass density,  $p$  is the fluid pressure,  $u^\mu$  is the fluid four-velocity, and  $\tilde{v}^k$  is the fluid velocity as measured by normal observers with four-velocity  $n_\mu = (-\alpha, \vec{0})$ ,  $\alpha = \sqrt{-1/g^{tt}}$ , with  $g^{\mu\nu}$  ( $g_{\mu\nu}$ ) the contravariant (covariant) components of the spacetime metric. The magnetic field is represented by  $B^k = {}^*F^{kt}$ , where  ${}^*F^{\mu\nu}$  is the dual of the Maxwell tensor times  $1/\sqrt{4\pi}$ ,  $b^\mu = (\delta_\nu^\mu + u^\mu u_\nu) B^\nu$  is the projection of the magnetic field into the fluid's co-moving frame. In addition,  $\Gamma^\lambda{}_{\mu\nu}$  is the affine connection and  $T^\mu{}_\nu$  is the sum of the stress-energy tensor of a perfect fluid and the EM stress energy tensor, defined as:

$$T_{\mu\nu} = (\rho h + 2p_m) u_\mu u_\nu + (p + p_m) g_{\mu\nu} - b_\mu b_\nu, \quad (6)$$

where  $h = 1 + \epsilon + p/\rho$  denotes the specific enthalpy,  $\epsilon$  the specific internal energy, and  $p_m = b^\mu b_\mu/2$  the magnetic pressure. The internal energy is  $u = \rho\epsilon$ , and we assume an adiabatic  $\Gamma$ -law equation of state:  $p = (\Gamma - 1)u$ .

The HANDOFF package can be extended to deal with more general formalisms. For instance, if using a realistic and finite-temperature equation of state, we can also include the electron fraction and temperature of the plasma. We will describe such extensions to the HANDOFF package in an forthcoming article, where we will transition a simulation from ILLINOISGRMHD to the numerical code HARM3D+NUC [81].

### B. BNS merger

We simulate the BNS merger with the numerical code ILLINOISGRMHD [79]. This code is implemented as a set of modules, or “thorns”, built upon the Cactus [83] and Carpet infrastructure [84, 85], within the Einstein Toolkit framework [86, 87]. Carpet enables ILLINOISGRMHD to sample the physical fields on Cartesian AMR numerical grids.

The integration in time of the conservation equations for the primitives  $\rho$ ,  $p$ , and  $\tilde{v}^k$  follows from high-resolution shock-capturing (HRSC) schemes. To be precise, ILLINOISGRMHD adopts the coordinate velocity  $v^k = u^k/u^0$  as a primitive instead of  $\tilde{v}^k$ . HRSC schemes, in a nutshell, reconstruct the primitive variables at the cell interfaces, solve for the fluxes with an approximate

Riemann solver, and integrate in time with the Method of Lines (MoL). The standard methods adopted are Piecewise Parabolic Method (PPM) [88] for the reconstruction of primitives, Harten-Lax-van Leer (HLL) for the approximate Riemann solver, and fourth-order Runge-Kutta (RK4) for the MoL integration.

The integration of the induction equation for  $B^k$  requires further care because the propagation of truncation errors can violate the solenoidal constraint  $\partial_i(\sqrt{-g}B^i) = 0$ . Constrained-transport schemes for  $B^k$  have proven to avoid these violations by finite-differencing the derivatives in the induction equation with specific stencils [see, for instance, 89], but their scope is limited to uniform grids, unless special steps or conditions are implemented. ILLINOISGRMHD instead evolves the vector potential  $A_k$  directly at staggered locations on a given cell, ensuring that results match those adopting a standard constrained-transport algorithm [90]. The algorithm is summarized as follows. The induction equation is recast as an evolution equation for  $A_k$ , which is integrated with HRSC methods, and then  $B^k$  is obtained from the curl of  $A_k$ , satisfying the solenoidal constraint to roundoff error [91].

After each time step, the primitive variables need to be recovered from the conserved variables in the conservative-to-primitive step. ILLINOISGRMHD adopts a Newton-Raphson-based 2D recovery scheme, which is also available in HARM3D [92]. This step can fail, however, if the conserved variables become invalid during the evolution. This happens most often in regions where high accuracy is difficult to maintain: the low density “atmosphere”, inside the BH horizon, or at AMR refinement boundaries. ILLINOISGRMHD enforces MHD inequalities that the conserved variables must satisfy in order to mitigate the number of recovery failures. If a failure still occurs, a backup primitive recovery method is used that is guaranteed to succeed, as described in Appendix A of [93].

The conservative-to-primitive step is prone to failure for lower densities of the artificial atmosphere. A typical value that results in robust, stable evolutions with small numbers of recovery failures is  $\rho_{\text{atm}}^{\text{Cactus}} \sim 10^{-8} \rho_{\text{max}}$ , where  $\rho_{\text{max}}$  is the maximum initial baryonic density. The minimum allowed value for the conserved energy used by ILLINOISGRMHD,

$$\tau \equiv \sqrt{-g} (\alpha T^{tt} - u^t \rho), \quad (7)$$

is obtained by assuming  $\rho = \rho_{\text{atm}}^{\text{Cactus}}$ , flat space, zero velocities, and zero magnetic fields, yielding

$$\tau_{\min} = \epsilon_{\text{atm}}^{\text{Cactus}} \rho_{\text{atm}}^{\text{Cactus}}, \quad (8)$$

where the “atmosphere” energy  $\epsilon_{\text{atm}}^{\text{Cactus}} = \epsilon(\rho_{\text{atm}})$  is computed using the gamma-law EOS with  $\Gamma = 2$  and  $K = 0.0332 \rho_{\text{nuc}} c^2 / n_{\text{nuc}}^{\Gamma} = 123.6$  (in code units), where  $\rho_{\text{nuc}}$  and  $n_{\text{nuc}}$  are the nuclear rest-mass and number densities, respectively. Empirically, we have determined that choosing an “atmosphere” value  $\tau_{\text{atm}}^{\text{Cactus}}$  up to  $\sim 10^2 \tau_{\min}$

(see Eq. (8)) leads to stable evolutions and accurate data transfers to HARM3D, while choosing values a few orders of magnitude larger can lead to an unstable transition.

During the BNS merger, the spacetime is highly dynamical and, besides integrating the equations of motion for the plasma, we need to integrate the equations of motion for the metric components  $g_{\mu\nu}$ . These equations are the Einstein field equations, written in the standard 3+1 Arnowitt-Deser-Misner (ADM) formalism [94], in the BSSNOK formulation [95–97]. In order to integrate these equations numerically, we use the thorn McLachlan [98] [99], which has been written with the Kranc [100] application.

### C. Grid design and export

Numerical errors rapidly sap angular momentum from fluid flows that obliquely cross coordinate lines. Thus continuing to model the dynamics of a post-merger BH accretion disk over timescales far longer than the inspiral/merger timescale with moderate-resolution Cartesian AMR grids would be ill-advised. Thus we choose a post-handoff grid that samples the remnant accretion disk in a spherical coordinate system designed specifically for modeling black hole accretion. The post-handoff grid is implemented within the same code adopted for post-handoff evolution: HARM3D.

To begin the handoff, HARM3D specifies the Cartesian coordinate locations of all cell-centers, lower-faces, and corners, for both physical and ghost cells on its spherical grid. The number of coordinates dumped, then, is  $(N^r + 2N_G) \times (N^\theta + 2N_G) \times (N^\phi + 2N_G) \times 3 \times 5$ , where  $N^r$ ,  $N^\theta$ , and  $N^\phi$  are the number of cells in each dimension,  $N_G$  is the number of ghost cells beyond each coordinate boundary,  $\times 3$  stands for each spatial dimension, and  $\times 5$  for each cell location.

In case the numerical codes assume different values for the unity of mass in geometrical units, we normalize the exported coordinates. For instance, if the unit of length of the destination grid equals the mass of the black hole remnant  $M_{\text{BH}}$ , but the unit of length during the merger equals  $M_{\odot}$ , then we multiply the exported coordinates of the destination grid by  $M_{\text{BH}}/M_{\odot}$ .

### D. Interpolation routine

In order to restart a GRMHD simulation in HARM3D we need two sets of grid-functions at a given time: the MHD primitives  $\mathbf{P}_{\text{HandOff}}$ , and the geometry of spacetime  $\mathbf{g}_{\text{HandOff}}$ . We have implemented a thorn [101] within the CACTUS infrastructure that reads in the Cartesian coordinates of the cell-positions of the destination grid and proceeds to interpolate both sets of grid-functions into them.

Specifically, regarding the first set  $\mathbf{P}_{\text{HandOff}}$ , we inter-

polate the following grid-functions:

$$\mathbf{P}_{\text{HandOff}} = \{\rho, p, \tilde{v}^r, \tilde{v}^\theta, \tilde{v}^\phi, A_x, A_y, A_z\}. \quad (9)$$

We require most of the values of  $\mathbf{P}_{\text{HandOff}}$  only at the cell-centers and, since their behaviour can be smooth or discontinuous, we use three different orders of Lagrangian interpolation: first, second, and fourth. The vector potential components  $A_k$  are an exception: To be consistent with the algorithms that calculate the curl of  $A_k$  in HARM3D, we interpolate the components of  $A_k$  into the corners of the destination cells. Further, we use third-order Hermite interpolation for  $A_k$  since it ensures continuity in the first derivatives of the interpolant function. Notice that, although we will transform the basis of tensorial quantities later in the HANDOFF, we transform the Cartesian velocities  $\{v^x, v^y, v^z\}$  to a spherical basis  $\{v^r, v^\theta, v^\phi\}$  before interpolation. In this way, we avoid the propagation of truncation errors of dominant components—usually  $\tilde{v}^\phi$ —into other components during the basis transformation.

Regarding the second set,  $\mathbf{g}_{\text{HandOff}}$ , consider that HARM3D does not evolve the spacetime metric, so the HANDOFF is limited to stationary geometries. Then  $\mathbf{g}_{\text{HandOff}}$  is simply given by the components of the four-dimensional metric in Cartesian coordinates:

$$\mathbf{g}_{\text{HandOff}} = \{g_{\mu\nu}^{\text{Cart}}, \mu, \nu = t, x, y, z\}. \quad (10)$$

We interpolate  $\mathbf{g}_{\text{HandOff}}$  to every cell-position and, since the metric components will be differentiated for the calculation of the affine connections, we use third-order Hermite interpolation that, as mentioned, ensures continuity in the first derivatives of the interpolant function.

Even in the equal-mass case, the collapsed BH after a BNS merger might have a gauge-induced velocity  $\tilde{v}_{\text{BH}}^i$ . We correct for this effect by applying the interpolation routine in the frame of the BH. Specifically, we shift  $x^i \rightarrow x^i - x_{\text{BH}}^i$  and  $\beta^i \rightarrow \beta^i + \tilde{v}_{\text{BH}}^i$  before calculating and interpolating  $\mathbf{P}_{\text{HandOff}}$  and  $\mathbf{g}_{\text{HandOff}}$ .

If the radial extent of the destination grid exceeds the boundaries of ILLINOISGRMHD’s grid, we set the grid-functions to an undefined value, or `NaN`, at the corresponding cells. Marking cells in this way ensures that they are easily found and their values overwritten with extrapolated data later in the HANDOFF procedure.

The interpolation routine returns a unique file in binary format where the values of each grid function in the destination grid are stored in contiguous memory locations.

### E. Parse dataset

With a standalone script, we parse the binary file that results from the interpolation routine, and construct restart files, readable by HARM3D. Specifically, we read each grid function and distribute it in an array of dimension  $(N^r + 2N_G, N^\theta + 2N_G, N^\phi + 2N_G)$ . We discard the

values of the primitives at the ghost cells as we will re-fill them at run-time based on the boundary conditions selected for the continued evolution. The vector potential  $A_k$  entails an exception: We need to keep its interpolated values at the ghosts cells in order to calculate its curl when initializing the continued run. We also keep the interpolated values of the metric at the ghost cells, since these will be required at initialization for calculating the spacetime connections in the physical cells next to the coordinate boundaries.

We dump these re-ordered arrays in three restart files, each containing a different interpolation order for the primitives  $\mathbf{P}_{\text{HandOff}}$ .

### F. Selective interpolation orders

The truncation errors in an interpolation scheme over a smooth function are proportional to  $\Delta x^{n+1}$ , where  $\Delta x$  denotes a measure of the grid resolution and  $n$  the order of the algorithm. Higher orders are preferred for smooth functions to minimize the truncation error. MHD primitives, however, might present strong shocks and discontinuities that induce Gibbs phenomena when using high interpolation orders. Our strategy in the HANDOFF is to keep higher-order results where the solution is smooth, but lower-order results where it is sharp. To that end, for each primitive, we take the results from the first-order interpolation, which is free of Gibbs phenomena, and we compare its local values to the averages over its neighboring cells ( $\pm 2$  cells in each dimension). If the relative error between these quantities is lower than 1%, we take the local result from the fourth-order interpolation, if it is higher than 10% we take the first-order result, and if it is in between, we take the second-order result. The final outcome of this step is a unique restart file that mixes first-, second-, and fourth-order results for the primitives  $\mathbf{P}_{\text{HandOff}}$ .

This step is crucial for the robustness and precision of the HANDOFF. During our testing stage, we found that higher-order methods can introduce Gibbs phenomena in the MHD primitives at the boundaries of handed-off accretion disks, leading to severe MHD perturbations and shocks that were not in the original simulation, and preventing a continuous transition between codes. On the other hand, using solely lower-order methods compromised the accuracy of the transition.

### G. Metric and primitives extrapolation

In case the outer boundary of the destination grid exceeds the outer boundary of the original grid, we extrapolate the geometry  $\mathbf{g}_{\text{HandOff}}$  and primitives  $\mathbf{P}_{\text{HandOff}}$  into the complementary cells.

Regarding the geometry  $\mathbf{g}_{\text{HandOff}}$ , we treat each of the ten independent components of the four-metric individually. Unlike the primitives  $\mathbf{P}_{\text{HandOff}}$ , the metric compo-

nents will generally take non-zero values everywhere in the computational domain, falling off as inverse polynomials of radius. To extrapolate each metric component  $g_{\mu\nu}$  out to the larger computational domain, we follow this procedure:

- Perform a low-order (up to  $(l, m) = (4, \pm 4)$ ) spherical harmonic mode-decomposition of the component at each radius  $r$  in the destination grid. The result is a radial array of mode coefficients  $g_{\mu\nu}^{(l,m)}(r) \equiv \oint g_{\mu\nu}(r, \theta, \phi) Y_{lm}(\theta, \phi) d\Omega$ .
- In a “trusted window”  $r \in \{R_1, R_2\}$ , perform a least-squares fit of each mode coefficient  $g_{\mu\nu}^{(l,m)}(r)$  to a power-law function  $a_0 + a_1/r^n$ .
- Construct a new radial array of coefficients that transitions continuously from the original numerical data to the power-law fit over the course of the trusted window:

$$\bar{g}_{\mu\nu}^{(l,m)}(r) = (1 - \lambda(r))g_{\mu\nu}^{(l,m)}(r) + \lambda(r)(a_0 + a_1/r^n),$$

where

$$\lambda(r) \equiv \begin{cases} 0 & r < R_1 \\ \frac{r-R_1}{R_2-R_1} & R_1 \leq r \leq R_2 \\ 1 & r > R_2 \end{cases}$$

- Use the power-law fit to generate  $g_{\mu\nu}^{(l,m)}(r)$  values for all  $r > R_2$ , extending to fill the full HARM3D domain.
- Finally, reconstruct  $g_{\mu\nu}(r, \theta, \phi)$  at every point in the larger domain using the new extended  $g_{\mu\nu}^{(l,m)}(r)$ .

For some individual modes, the power-law functional least-squares fit may fail to converge—generally a symptom of that mode being dominated by low-amplitude noise. In these cases, we keep the original mode data out to  $R_2$ , and use the value at  $r = R_2$  to fill the remainder of the domain—equivalent to setting  $a_0 = g_{\mu\nu}^{(l,m)}(R_2)$ ,  $a_1 = 0$ .

After extrapolating the metric components, we proceed to extrapolate the primitives  $\mathbf{P}_{\text{HandOff}}$ . We fill the complementary cells with the numerical atmosphere of HARM3D,  $\rho = \rho_{\text{atm}}$ ,  $u = u_{\text{atm}}$ , where  $\rho_{\text{atm}}, u_{\text{atm}}$  are defined below, and we set the rest of the primitives to zero.

To avoid a sharp transition between the numerical atmospheres of ILLINOISGRMHD and HARM3D at the the boundary between the handed-off and extrapolated primitives, we also adjust the handed-off atmosphere. If  $\rho < 1.1 \times \rho_{\text{atm}}^{\text{Cactus}}$ , we set  $\rho = \rho_{\text{atm}}$ ,  $u = u_{\text{atm}}$ , and keep the rest of the primitives unchanged.

## H. Continued evolution

At this stage we have a restart file in a format readable by HARM3D that contains the MHD primitives at the physical cell centers, the vector potential  $A^k$  at the corners of physical and ghost cells, and the metric at all cell positions for all cells. Using existing restart routines, we read in and distribute the MHD primitives among different processors in HARM3D. The vector potential and metric components require specific routines that take into account the ghost-cells and different cell positions when reading-in and distributing its values.

We transform the metric and vector potential components from the Cartesian basis to the numerical basis of the destination grid:

$$g_{\mu'\nu'} = \frac{dx_{\text{Cart}}^\alpha}{dx^{\mu'}} \frac{dx_{\text{Cart}}^\beta}{dx^{\nu'}} g_{\alpha\beta}^{\text{Cart}}, \quad (11)$$

$$A_{\mu'} = \frac{dx_{\text{Cart}}^\alpha}{dx^{\mu'}} A_\alpha^{\text{Cart}}, \quad (12)$$

and we transform the velocity from the spherical basis to numerical:

$$\tilde{v}^{\mu'} = \frac{dx^{\mu'}}{dx_{\text{sph}}^\alpha} \tilde{v}_{\text{sph}}^\alpha. \quad (13)$$

We calculate the curl of the vector potential  $A_k$  with standard routines in HARM3D and obtain the magnetic field  $B^k$  at the cell-centers, maintaining the solenoidal constraint [102]. We also calculate the affine connections for the numerical metric with standard routines of HARM3D. These use fourth-order (second-order) finite differences for spatial (temporal) derivatives of the metric to obtain the Christoffel symbols; cell extents are used as the discrete spacing in the spatial finite differences, while a much smaller time spacing than the evolution’s Courant-limited time step is used in order to keep its truncation error smaller than that of the spatial difference. We typically limit the simulations from handed-off ID to instances when the metric is nearly stationary, so the continued evolution is assumed to have a time-independent spacetime. For this reason during HAND-OFF we simply use the same metric field data for all nominal time slices fed into the HARM3D affine connection routine, guaranteeing that all temporal derivatives will be zero.

We evolve the handed-off primitives over the numerical spacetime in the destination grid with the well-tested methods of HARM3D [80, 81, 103]. We integrate the equations of motion, Eq. (1), with HRSC schemes. We reconstruct the primitive variables to the cell interfaces through piecewise parabolic interpolation, we apply the Lax-Friedrichs formula to compute the local fluxes, and the method of lines for time integration with a second-order Runge-Kutta (RK2) method. The primitive variables are recovered from the conserved variables with

the scheme described in [92] and [81]. If the updates of  $\rho$  or  $u$  go below the corresponding atmosphere values  $\rho_{\text{atm}} = 2 \times 10^{-10}(r/M)^{-3/2}$ ,  $u_{\text{atm}} = 2 \times 10^{-12}(r/M)^{-5/2}$  they are reset to the latter. We use the constrained transport algorithm FluxCT [89] to evolve the magnetic field  $B^k$  and maintain the solenoidal constraint. For more details, see Ref. [80].

### III. CODE VERIFICATION: FISHBONE-MONCRIEF DISK

To verify the HANDOFF we take the case of a magnetized Fishbone-Moncrief disk [FM; 104] around a rotating BH. We evolve the system with ILLINOISGRMHD and HARM3D independently, and we use the HANDOFF to perform several transitions between the codes at different stages of the simulation.

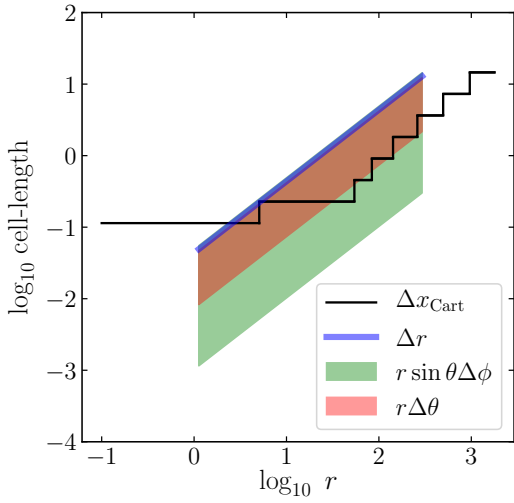


FIG. 2. Cell-lengths as a function of radii for the FM simulations in ILLINOISGRMHD (black) and HARM3D (green, red, and blue). Shaded regions show how the cell lengths change over the full span of  $\theta$ . Note that regions of overlap between green and red appear brown in the plot.

We begin by setting the same initial data in ILLINOISGRMHD and HARM3D for a magnetized FM disk around a BH of mass  $M$  with specific angular momentum  $a/M = 0.9375$ , as dictated by Ref. [105]. We evolve this data with ILLINOISGRMHD and HARM3D up to  $t = 10^4 M$ . The grid in ILLINOISGRMHD consists of a Cartesian hierarchy of 8 refinement levels, as described in Ref. [105]. The grid in HARM3D has a spherical topology and consists of  $128^3$  cells, parametrized by numerical coordinates that refine the resolution towards the equator and towards the BH, with the functional dependence used by Ref. [106] (we use  $h = 0.3$  in Eq. (8) of this reference). We make use of novel boundary conditions at the coordinate boundaries of  $\theta$ , i.e. at the polar axis, which allow us to fully extend  $\theta \in (0, \pi)$ . In Appendix B we

describe the details of these boundary conditions. The coordinate boundaries of  $\phi$  are internal to the domain, and the coordinate boundaries of  $r \in [1.1M, 300M]$  are physical boundaries, where we impose outflow boundary conditions.

In Fig. 2 we plot the cell-lengths in both ILLINOISGRMHD and HARM3D as a function of radii and for  $\theta \in (0, \pi)$ , and conclude the resolutions are comparable. The cell-length  $\Delta r$  grows as a function of radius because the radial resolution has an exponential dependence with radius. The cell-length  $r \sin \theta \Delta \phi$  grows as a function of radius because of its explicit radial dependence, and also spans different values at each radius because of its  $\theta$  dependence. Finally the cell-length  $r \Delta \theta$  grows as a function of radius because of its explicit radial dependence and has different values for a given radius because  $\Delta \theta$  is not uniform, but progressively *smaller* toward the equator.

As can be seen from Fig. 2, the numerical domain in HARM3D is contained in the domain in ILLINOISGRMHD, therefore we do not need to extrapolate the primitives or metric (see Sec. II G). We will validate the extrapolation procedure in the next section, where we apply the HANDOFF to a BNS post-merger.

We do the first transition at  $t = 0$ , i.e. we hand off the initial data (ID) from ILLINOISGRMHD to HARM3D. By comparing the resulting data-set with the ID constructed in HARM3D, we can measure the truncation error introduced in the HANDOFF. Based on the resolution of ILLINOISGRMHD in the region of the disk  $\Delta x_{\text{IGM}} \approx 0.2274$ , and the interpolation orders considered  $n = 1, 2, 3, 4$ , we expect the following values for the truncation errors

$$\epsilon \sim \Delta x_{\text{IGM}}^{n+1} \sim \begin{cases} 5 \times 10^{-2}, & n = 1 \\ 1 \times 10^{-2}, & n = 2 \\ 2 \times 10^{-3}, & n = 3 \\ 6 \times 10^{-4}, & n = 4 \end{cases}. \quad (14)$$

In Fig. 3 (*left*) we plot the interpolation orders selected for the primitive  $\rho$ , in the  $xz$ -plane. The distribution follows the expected behavior: At the core of the disk, around the position of the maximum of pressure at  $r = 12M$ , fourth-order interpolation is selected. In contrast, at the surface of the disk, where the density jumps to the value of the numerical floor, first-order is selected. There is also a transition region in the body of the disk where second-order is selected.

In Fig. 3 (*right*) we plot  $\epsilon_R[\rho]$  in the  $xz$ -plane, where

$$\epsilon_R[P] = \frac{|P_{\text{harm3d}} - P_{\text{HandOff}}|}{\frac{1}{2}(|P_{\text{harm3d}}| + |P_{\text{HandOff}}|)} \quad (15)$$

is the relative error between the handed-off primitive and the value initialized in HARM3D. As expected from the estimates in Eq. (14), the body of the disk presents  $\epsilon_R[\rho] \sim 1 \times 10^{-4}$  and transitions to  $\epsilon_R[\rho] \sim 1 \times 10^{-2}$  near the surface of the disk. The region around the BH with higher errors happens because ILLINOISGRMHD sets a tenuous atmosphere with  $\rho > 1.1\rho_{\text{atm}}^{\text{Cactus}}$  around the BH

and the HANOFF does not reset it to the HARM3D's atmosphere. This is still a low-density region, where  $\rho < 1 \times 10^{-5}$  in code units, and it does not affect our results. In global terms, the density-weighted relative error  $\langle \epsilon_R[\rho] \rangle_\rho$ , where

$$\langle X \rangle_\rho = \frac{\int X \rho \sqrt{-g} dV}{\int \rho \sqrt{-g} dV}, \quad (16)$$

is  $\langle \epsilon_R[\rho] \rangle_\rho = 2 \times 10^{-4}$ .

For the remaining primitives, we find equivalent distributions for the interpolation orders selected, but different values for the integrated errors. We find a higher integrated error for the internal energy  $\langle \epsilon_R[u] \rangle_\rho = 1 \times 10^{-2}$  but this is dominated by random perturbations, introduced artificially to trigger accretion. We find lower errors for non-vanishing components of the velocity  $\langle \epsilon_R[v^{(1)}] \rangle_\rho = 8 \times 10^{-6}$  and  $\langle \epsilon_R[v^{(3)}] \rangle_\rho = 1 \times 10^{-5}$ . These functions are smoother than  $\rho$ , and monotonically decrease in  $r$  within the disk, explaining why the interpolation is more accurate. We find higher errors for the non-vanishing components of the magnetic field  $\langle \epsilon_R[B^{(1)}] \rangle_\rho = \langle \epsilon_R[B^{(2)}] \rangle_\rho = 1 \times 10^{-1}$  that come from the propagation of truncation errors in  $A_k^{\text{Cart}}$  after the basis transformation and curl calculation. Regarding the primitives that are initialized to zero, we define the relative error by

$$\tilde{\epsilon}_R[P] = |P_{\text{HandOff}}| \quad (17)$$

and find  $\langle \tilde{\epsilon}_R[v^{(2)}] \rangle_\rho = 5 \times 10^{-19}$  and  $\langle \tilde{\epsilon}_R[B^{(3)}] \rangle_\rho = 4 \times 10^{-8}$ . Comparing  $\langle \tilde{\epsilon}_R[v^{(2)}] \rangle_\rho$  with  $\langle \tilde{\epsilon}_R[B^{(3)}] \rangle_\rho$  we notice the convenience of transforming to the spherical basis before interpolation and the effect of error propagation by the curl calculation. In the case of the BNS post-merger, however, we expect these errors on the magnetic field components to be smaller, since the different components, and therefore the truncation errors, will be more comparable in magnitude.

In this validation test, we can also measure the truncation errors of the handed-off metric components, since we know their analytical values in advance. Overall, we find lower errors for the metric components than for the MHD primitives,  $\langle \epsilon_R[g_{\mu\nu}] \rangle_\rho < 1 \times 10^{-7}$ . These lower errors in the metric components were expected because these are differentiable functions, and because we use third-order interpolation in every cell.

After confirming that the handed-off ID and spacetime metric are consistent with our expectations, we evolve the data-set within HARM3D. We denote this simulation `HandOff_0`.

Defining the accretion rate as

$$-\frac{dM}{dt}(r) = \int \rho u^r \sqrt{-g} d\theta d\phi, \quad (18)$$

in Fig. 4 (top) we plot this quantity at the BH horizon for `HandOff_0` (green) and for the fiducial run in HARM3D

(light blue). We also include the accretion rate for the fiducial run in ILLINOISGRMHD (orange). We notice the evolution of `HandOff_0` is dynamically equivalent to the fiducial run in HARM3D, capturing the MRI growth, saturation, and relaxation.

To test the HANOFF in a more realistic and turbulent scenario, we transition the same simulation from ILLINOISGRMHD to HARM3D at  $t = 4.1 \times 10^3 M$ . We denote this continued evolution `HandOff_1`. In Fig. 4 (top, red) we plot the resulting accretion rate and, again, we find the HANOFF successfully captures the dynamical state of the disk, reproducing the value of the accretion rate at the time of transition, and the spike in the accretion rate at  $t \sim 5 \times 10^3 M$ .

Finally, we perform a transition at  $t = 8.1 \times 10^3 M$  and we denote this continued evolution `HandOff_2`. In Fig. 4 (top, violet) we plot the resulting accretion rate and we notice its value at the transition time matches the value in ILLINOISGRMHD, proving a continuous transition. The accretion rate then converges to the results of HARM3D. Indeed, while the state of the disk at the transition time is determined by ILLINOISGRMHD, the continued evolution is determined by the numerical methods in HARM3D. The drop in the accretion rate was expected for the lower numerical dissipation and better conservation of angular momentum in spherical grids for azimuthal flows.

Beyond the local measure of the accretion rate, we analyze the continuity of global quantities after the HANOFF. In Fig. 4 (bottom) we plot the integrated mass of the disk within  $r = 100M$ , normalized by the initial mass  $M_0$ . We find the curves of `HandOff_0`, `HandOff_1` and `HandOff_2` match the results from ILLINOISGRMHD at the time of transition, proving the high fidelity of the HANOFF.

We conclude the HANOFF successfully translates the GRMHD state of a magnetized torus, and the space-time metric, from a Cartesian-AMR grid within ILLINOISGRMHD to a more flexible grid within HARM3D. In the next section we will apply the HANOFF to the interesting case of a BNS post-merger.

## IV. RESULTS: BNS POST-MERGER

In this section we evolve a BNS merger with ILLINOISGRMHD and apply the HANOFF to continue the post-merger evolution in HARM3D. The results presented in this section are well-known from the literature, but serve to demonstrate the consistency and validity of the continued evolution from the HANOFF.

### A. Merger proper

The ID for the BNS is similar to that of [58] [see also Refs. 64, 66, for similar settings]: Two NSs in a circular orbit, separated by  $\sim 45$  km, each with a gravitational

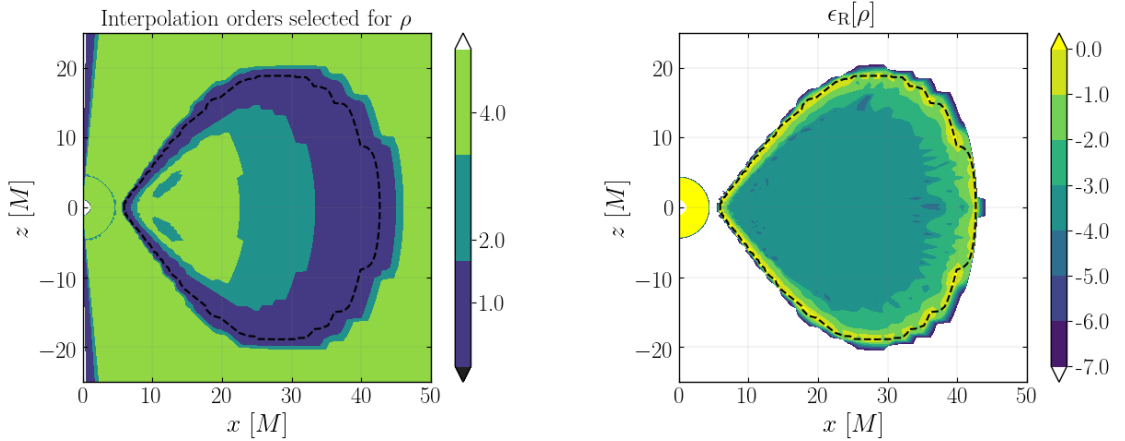


FIG. 3. Interpolation orders selected (*left*) and the corresponding relative errors (*right*) for  $\rho$ , when handing-off ID for a magnetized FM from ILLINOISGRMHD to HARM3D. Fourth-order interpolation is selected at the core of the disk where  $\rho$  is smooth, and first-order is selected at the surface of the disk where there is a jump to the numerical floor. There is also a transition region where second-order interpolation is selected. The numerical errors follow the expected values from the resolution and interpolation orders (see Eq. (14)).

mass of  $1.5 M_{\odot}$  and an equatorial radius of 13.6 km. We also initialize two poloidal magnetic fields, confined in each star, but with a maximum strength of  $\sim 10^{15}$  G, three orders of magnitude higher than in Ref. [58]. We use a Cartesian-AMR grid centered in the center of mass of the system, with outer boundaries at  $\sim 5700$  km, and 7 refinement boundaries with a finest resolution of  $\sim 180$  m. We model the fluid as an ideal gas, with adiabatic index  $\Gamma = 2$ .

We evolve this ID with ILLINOISGRMHD and, consistent with Ref. [58], we find the NSs inspiral towards the center of mass of the system as they transfer energy and angular momentum to gravitational waves (GW), until they merge after 8 ms ( $\sim 3$  orbits). After merger, a HMNS forms but, given the large mass of the system, it promptly collapses to a BH ( $\sim 8$  ms after merger). If we set the ID at time  $t = 0.0$  s, then the BH forms at  $t_{\text{BH}} = 0.017$  s. We use the thorn `AHFinderDirect` [107] to locate the apparent horizon; the resulting BH has a mass of  $2.911 M_{\odot}$ , a specific angular momentum of 0.82, and a drift velocity  $v_{\text{BH}} \sim 1 \times 10^{-3}c$ . At  $t = t_{\text{BH}}$ , we add two refinement levels centered at the remnant, yielding a finest resolution after merger of  $\sim 50$  m. The remnant is surrounded by an orbiting and magnetized torus, with mass  $0.076 M_{\odot}$ .

## B. Handing-off the post-merger: destination grids and boundary conditions

After BH formation, we apply the `HANDOFF` and transition the BH-torus system to HARM3D. For consistency checks, we do the transition at different times and to different grids.

We do the first `HANDOFF` at  $t_0 = 0.020$  s, 0.003 s after BH formation, and use a grid equivalent to that

of Ref. [108], but with  $\xi = 0.65$ ,  $\theta_c \sim 1 \times 10^{-14}$ , and  $n = 7$  (see Eq. (22) of that reference), we set the radial extent  $r \in (1.07, 4291.53)$  km, and use  $1024 \times 160 \times 256$  cells. This grid is contained in the original grid for the merger, so we do not need to extrapolate the primitives or spacetime metric. We denote this transition, and continued evolution, `BNS_SmallRout_t0`. Using this same grid, we do a later transition, at  $t_1 = 0.032$  s, denoted `BNS_SmallRout_t1`. In Fig. 6 we plot the mass of the BH remnant  $M_{\text{BH}}$  as a function of time, calculated with the thorn `QuasiLocalMeasures` [109], and notice that  $M_{\text{BH}}$  is in a converging regime at times  $t_0$  and  $t_1$ . Specifically,  $M_{\text{BH}}(t_0) = 2.895 M_{\odot}$  and  $M_{\text{BH}}(t_1) = 2.911 M_{\odot}$ .

Next, we do a transition at the same time  $t_1$ , but to a grid designed specifically for a BNS post-merger. As described in the Introduction, this new grid has spherical topology, the outer boundary is far enough ( $\sim 10^5$  km) to capture the jet-breakout, it has higher resolution in  $\theta$  towards the equator if close to the BH to resolve the disk, but higher resolution towards the polar axis if farther away, to resolve the funnel region. The implementation details of this grid are described in Appendix A. In this case, since the destination grid is much larger than the original grid for the merger, we need to extrapolate the primitives and spacetime metric to the complementary cells. We denote this run `BNS_LargeRout_t1`, and consider it our fiducial simulation.

In Fig. 5 we include plots for the cell-lengths of these grids as a function of radii and for  $\theta \in (0, \pi)$ , compared with the resolution in ILLINOISGRMHD. We notice that, at the bulk of the disk ( $r < 200$  km), cells at the equator have higher resolution for both  $\theta$  and  $r$  with respect to the original resolution in ILLINOISGRMHD, and comparable resolution for  $\phi$ . The description of Fig. 5 (*left*) is similar to that of Fig. 2 in the previous section, for an exponential grid in  $\Delta r$  with  $\Delta\theta$  focused in the equator.

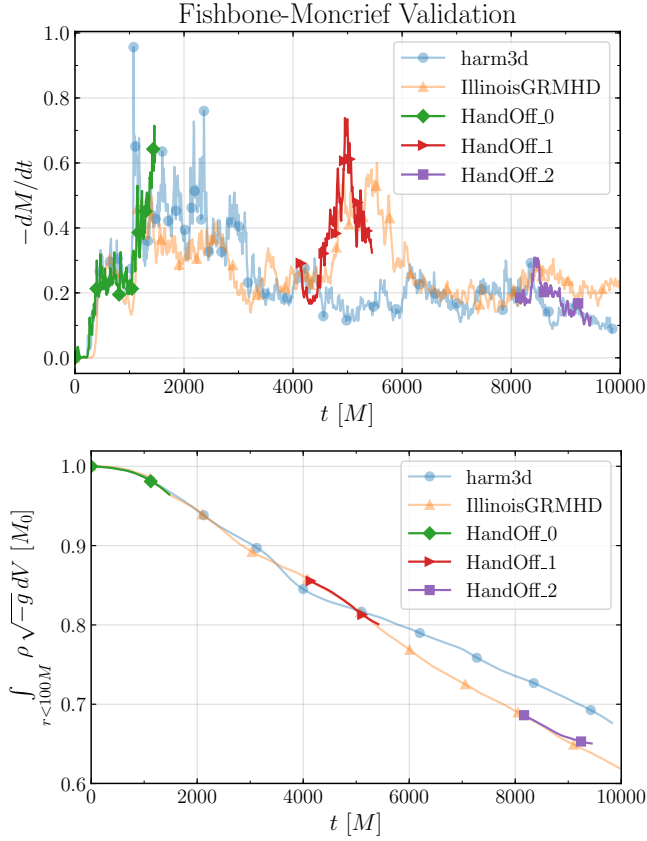


FIG. 4. Accretion rate at the horizon (top) and total mass within  $r = 100M$  (bottom) as a function of time for the FM validation case. The curves `harm3d` and `ILLINOISGRMHD` stand for the fiducial simulations with these codes. The curves `HandOff_0`, `HandOff_1` and `HandOff_2` represent handed-off runs from `ILLINOISGRMHD` to `HARM3D`, at times  $t = 0, 4.1 \times 10^3, 8.1 \times 10^3 M$ , respectively. In every case, the transition is continuous and the evolved system follows the expected behaviour from the fiducial runs.

The description of Fig. 5 (right) is more subtle and is given in Appendix A.

In every case, we apply novel boundary conditions of `HARM3D` at the polar axis that refer to neighbouring cells in the domain, allowing us to extend  $\theta \in (0, \pi)$  and to fully resolve the funnel region. See Appendix B for the details on implementing these boundary conditions. The coordinate boundaries of  $\phi$  are also internal to the domain, and the coordinate boundaries of  $r$  are the actual physical boundaries, where we impose outflow boundary conditions.

### C. Handing-off the post-merger: initial data

In Fig. 7 we plot the rest-mass density  $\rho$  in the  $x - z$  plane at the time of transition for `BNS_LargeRout_t1` (bottom). We also plot the original data from `ILLINOISGRMHD` (top), and we plot grey lines that represent the

grid topology for each case. As a demonstration of the precision of the `HANDOFF`, we note the plots of  $\rho$  are indistinguishable between the two codes.

In Fig. 8 we focus on the accretion disk around the remnant for `BNS_LargeRout_t1` (*solid, blue*), and plot the  $\theta$ -integrated and  $\phi$ -averaged density:

$$\Sigma(r) = \frac{\int \sqrt{-g} \rho d\theta d\phi}{\int \sqrt{g_{\phi\phi}}(\theta = \pi/2) d\phi}, \quad (19)$$

and the  $\phi$ -averaged specific angular momentum  $\hat{l}(r, \theta = \pi/2)$  and specific entropy  $\hat{s}(r, \theta = \pi/2)$  at the equator, where  $l = u_\phi/u_t$ ,  $s = \ln(p/\rho^\Gamma)$ , and

$$\hat{X}(r, \theta) = \frac{\int X \sqrt{g_{\phi\phi}} d\phi}{\int \sqrt{g_{\phi\phi}} d\phi}. \quad (20)$$

Since many references initialize the post-merger disk with an FM distribution [e.g. 110], or similar isentropic solutions with constant specific angular momentum, in Fig. 8 we also plot the latter quantities for the FM disk evolved in the previous section at  $t = 0$  (*dashed, orange*) and  $t = 9000M$  (*solid, orange*). For the FM, we set the unit of length assuming the central BH has a mass of  $2.911 M_\odot$ , and set the units of MHD variables assuming the code units are the same as in the BNS case. Comparing the post-merger disk with the curves for the evolved FM disk, we notice a steeper decay of  $\Sigma(r)$  in the post-merger case. The angular momentum of the post-merger is rather constant at the bulk of the disk, but presents a peculiar decreasing trend. The specific entropy, on the other hand, presents the most remarkable difference. For the post-merger disk, it grows steeply outwards because of the shocked and ejected material from the merger.

The accretion disk is fairly magnetized. At the time of transition, for `BNS_LargeRout_t1`, we find the ratio of the  $\rho$ -weighted integrals of thermal and magnetic pressure to be:

$$\frac{\int p \rho \sqrt{-g} dV}{\int p_m \rho \sqrt{-g} dV} \sim 140 \quad (21)$$

For comparison, we find this ratio to be  $\sim 560$  and  $\sim 30$  for the the FM evolved in the last section, at  $t = 0$  and  $t = 9000M$ , respectively. Therefore, according to this parameter, the magnetization of the relaxed FM is  $\times 4 - 5$  larger than the initial post-merger disk. In the next subsection we analyze the evolution of this parameter.

We proceed to investigate the topology of the magnetic field. Following [111], the decomposition of the magnetic field into toroidal  $B_{||}$  and poloidal  $B_{\perp}$  components for non-axysymmetric distributions of matter follows from the projection of the field with respect to the fluid frame:

$$B^i = B_{||} \frac{\tilde{v}^i}{\sqrt{\gamma_{ij} \tilde{v}^i \tilde{v}^j}} + B_{\perp}^i. \quad (22)$$

Then the magnetic energy can be decomposed into toroidal and poloidal components  $E_{\text{mag}} = E_{\text{mag}}^{||} + E_{\text{mag}}^{\perp}$ ,

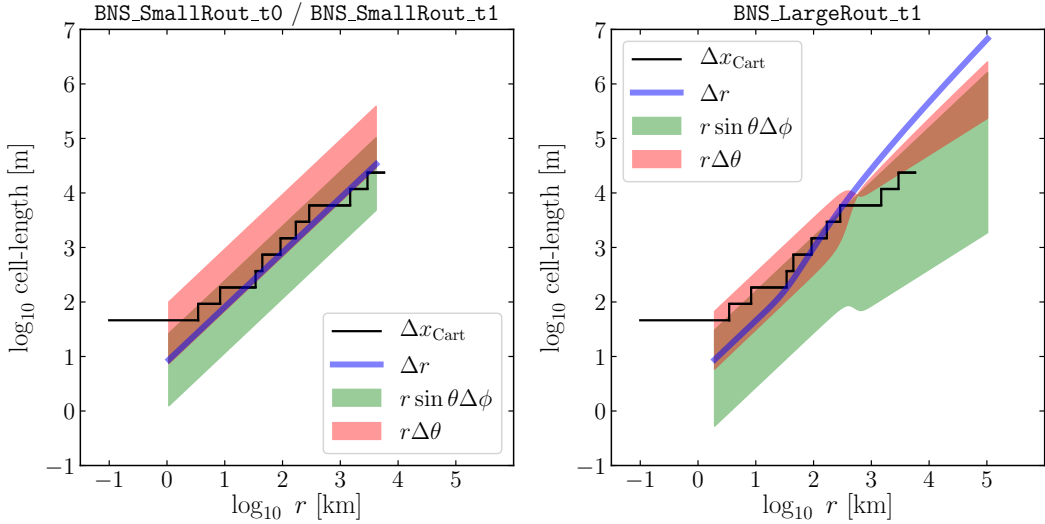


FIG. 5. Cell-lengths for BNS post-merger simulations as a function of radii. The *black* line represent the resolution of the AMR-levels used during merger. *Green*, *red*, and *blue* points represent the grid lengths for spherical-like cells used during the continued evolution in *BNS\_SmallRout\_t0* (*left*), *BNS\_SmallRout\_t1* (*left*), and *BNS\_LargeRout\_t1* (*right*).

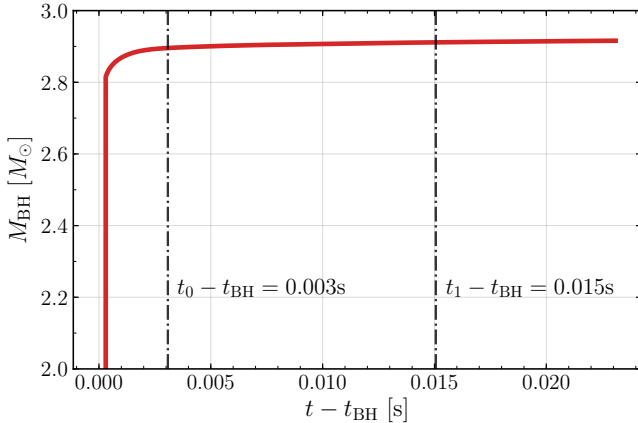


FIG. 6. Mass of BH remnant from the BNS merger, as a function of time. *Dashed-dotted* lines represent the times at which we apply the *HANDOFF*. For our fiducial run,  $M_{\text{BH}}(t_1) = 2.911 M_{\odot}$ .

where these quantities can be computed independently as

$$E_{\text{mag}} = \int T_{\text{EM}}^{00} \alpha \sqrt{-g} dV, \quad (23)$$

$$E_{\text{mag}}^{\parallel} = \int \frac{1}{2} B_{\parallel} B_{\parallel} \frac{\sqrt{-g}}{\alpha} dV, \quad (24)$$

$$E_{\text{mag}}^{\perp} = \int \frac{1}{2} g_{ij} B_{\perp}^i B_{\perp}^j (1 + g_{ij} \tilde{v}^i \tilde{v}^j) \frac{\sqrt{-g}}{\alpha} dV. \quad (25)$$

At the time of transition, for *BNS\_LargeRout\_t1*, we find  $E_{\text{mag}} = 3.136 \times 10^{48}$  erg, with  $E_{\text{mag}}^{\parallel} = 2.417 \times 10^{48}$  erg

and  $E_{\text{mag}}^{\perp} = 7.192 \times 10^{47}$  erg, i.e. we find the toroidal field is dominant. As a comparison, for the FM case, at  $t = 0$  and  $t = 9000M$ , respectively, we find  $E_{\text{mag}} = 1.197 \times 10^{53}$  erg,  $1.928 \times 10^{55}$  erg, with  $E_{\text{mag}}^{\parallel} = 1.297 \times 10^{52}$  erg,  $9.497 \times 10^{54}$  erg and  $E_{\text{mag}}^{\perp} = 1.067 \times 10^{53}$  erg,  $9.791 \times 10^{54}$  erg, i.e. it transitions from poloidal dominance to equipartition. Recall we have freedom of scale over the system of units in the FM disk, so only relative comparisons of  $E_{\text{mag}}$ ,  $E_{\text{mag}}^{\parallel}$ ,  $E_{\text{mag}}^{\perp}$  within each run are meaningful.

In addition to the accretion disk, the ID obtained from the *HANDOFF* includes the unbound debris from the merger (i.e., the dynamical ejecta). There are two main mechanisms of mass ejection during the merger, tidal interactions and shock heating [see, for instance, Ref. 112]. While the first mechanism predominantly expels cool material from the NSs to the orbital plane of the binary, the second ejects heated material quasi-isotropically. In Fig. 9 we visualize the dynamical ejecta for *BNS\_LargeRout\_t1* by plotting the specific entropy, along with dashed lines that contain the ejected material. We identify the ejecta as the parcels of fluid that are unbound, satisfying  $(h + b^2/\rho)u_t < -1$ , and move outwards, satisfying  $v^r > 0$ . Indeed, we recognize regions with low entropy around the equator, which we associate with the early tidal ejecta, and a quasi-spherical region with higher entropy, which we associate with the shocked-heated ejecta. We find the total ejecta have a mass of  $0.002 M_{\odot}$ , and an average radial velocity of  $0.15c$ . These values are consistent with the ranges found in the literature [37, 46, 112], supporting the validity of our methods. Regarding our specific model, the total mass of the ejecta is likely to be overestimated since we do not take neutrino cooling into account and this excess of internal

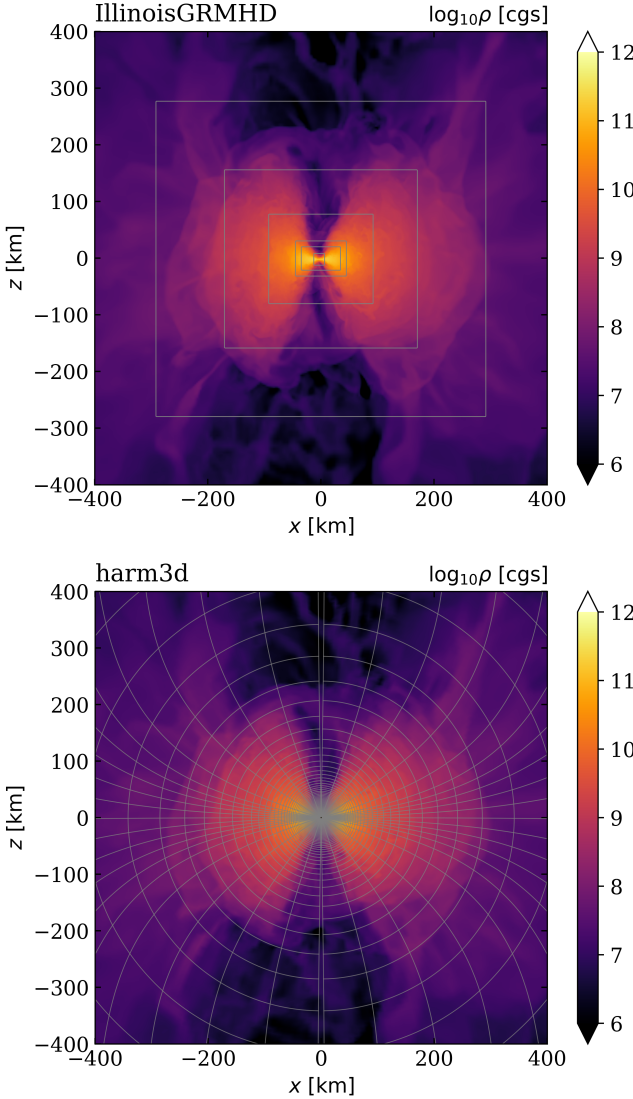


FIG. 7. Baryonic density  $\rho$  in the  $xz$ -plane for `BNS_LargeRout_t1` before (top) and after (bottom) the hand-off procedure, in ILLINOISGRMHD and HARM3D, respectively. The grey lines in the plot for ILLINOISGRMHD represent the AMR boundaries and, in the plot for HARM3D, they represent 1 every 10 grid-lines of the destination grid.

energy increases the amount of unbound material [36].

As mentioned, the destination grid of `BNS_LargeRout_t1` has its outer boundary much farther away than the original grid of ILLINOISGRMHD. Then, as described in Sec. II G, we need to extrapolate the primitives and spacetime metric. For the “trusted window” in the extrapolation of the spacetime metric, we use  $R1 = 500M_\odot$  ( $\sim 750$ km) and  $R2 = 800M_\odot$  ( $\sim 1200$ km). To test the validity of the extrapolated geometry, in Fig. 10 we plot the Hamiltonian constraint for the extrapolated metric in the  $x$ -axis, along with the constraint for the evolved metric in ILLINOISGRMHD at the time of transition. For the extrapolated metric,

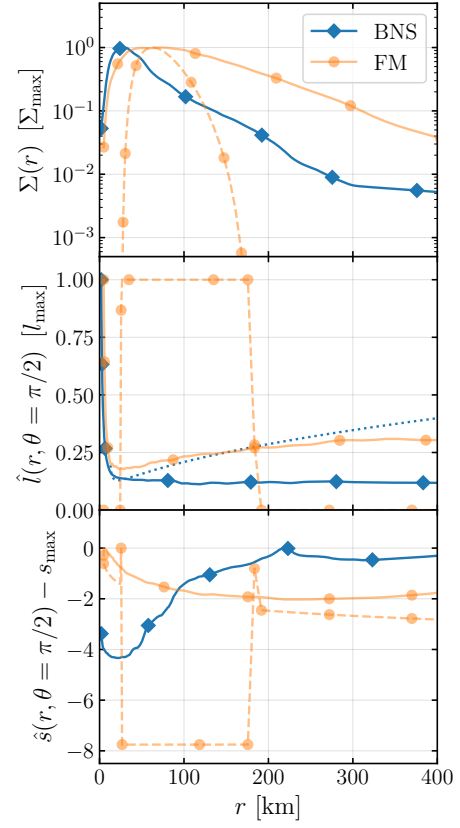


FIG. 8. Disk measures for `BNS_LargeRout_t1` at the time of transition (solid, diamond, blue), and for the FM disk evolved in Sec. III at  $t = 0$  (dashed, circle, orange) and  $t = 9000M$  (solid, circle, orange). From top to bottom, we plot the  $\theta$ -integrated and  $\phi$ -averaged density  $\Sigma(r)$ , the specific angular momentum at the equator  $\hat{l}(r, \theta = \pi/2)$ , and specific entropy at the equator  $\hat{s}(r, \theta = \pi/2) - s_{\max}$ . The blue, dotted line in the middle panel represent the Keplerian value for  $\hat{l}(r, \theta = \pi/2)$ , given the mass and spin of the remnant BH.

we neglect the contribution of matter to  $\mathcal{H}$  as the distribution of matter in this region is composed of the numerical atmosphere, with negligible energy. We find the values of  $\mathcal{H}$  for the extrapolated metric to be comparable to the values for ILLINOISGRMHD in the portion of the domain containing the expanding ejecta. In the next sub-section we will show that the evolution of the MHD fields in the extrapolated spacetime has the expected physical behaviour, and matches the results from `BNS_SmallRout_t1`, where extrapolation is not required and the numerical metric is taken directly from interpolation. In particular, we will compare the radial velocity  $v^r$  of the expanding ejecta of `BNS_LargeRout_t1` in the extrapolated region with those results for `BNS_SmallRout_t1`.

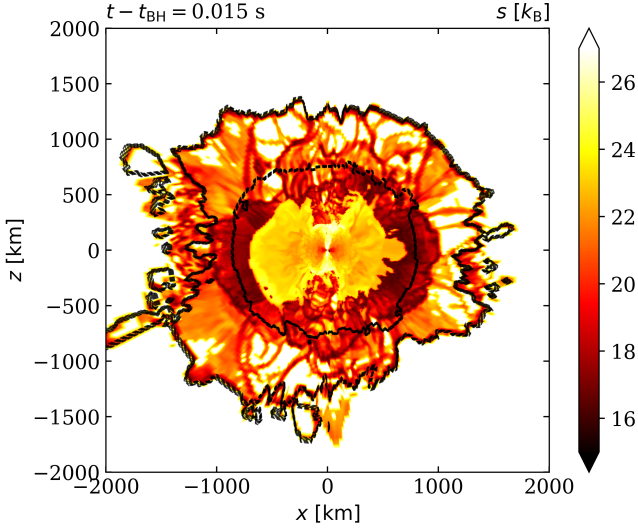


FIG. 9. Specific entropy of dynamical ejecta for BNS\_LargeRout\_t1. Unbound matter with outgoing radial velocity is enclosed within *black, dashed* curves.

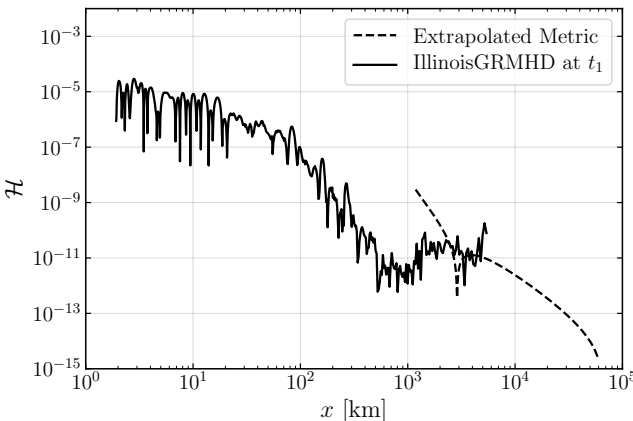


FIG. 10. Hamiltonian constraint  $\mathcal{H}$  at the  $x$ -axis at the time of transition for BNS\_LargeRout\_t1. We plot both the constraints for the evolved metric in ILLINOISGRMHD (*solid*), and for the extrapolated metric (*dashed*).

#### D. Handing-off the post-merger: continued evolution

We evolve BNS\_LargeRout\_t1 in HARM3D for 0.1 s, i.e. up to 0.115 s after BH formation. As we describe below, during this period we find the BH accretes  $0.023 M_{\odot}$  ( $\sim 27\%$  of the initial mass of the torus), the accretion rate converges to  $\sim 0.1 M_{\odot} s^{-1}$ , the magnetic energy increases by  $\sim 50\%$ , and the ejecta expand freely. We do not find significant magnetic outflows from the ergosphere of the remnant. We could have evolved the system for longer, but were limited by computational resources. We used 229 nodes of the supercomputer **Frontera** [113], for approximately 5 days, implying a system usage of almost

30k SUs (System Units). Considering that the number of cells is  $1024 \times 200 \times 400$  (see Appendix A), and that each node has 56 processors, our code runs at a pace of almost 70k cell updates per second per processor. For consistency checks, we also evolve BNS\_SmallRout\_t0 and BNS\_SmallRout\_t1 for approximately 0.04 s.

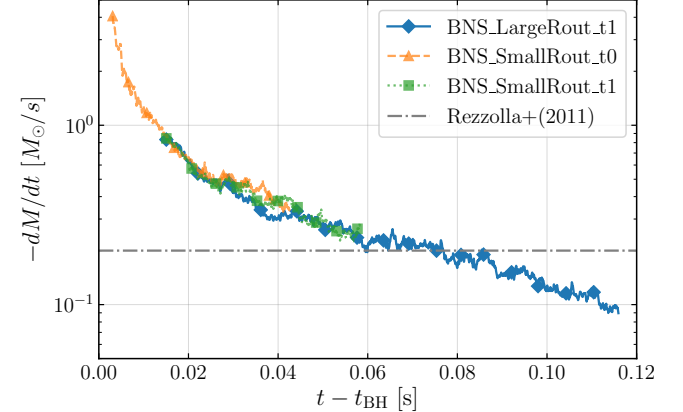


FIG. 11. Accretion rate at the horizon for the BNS post-merger simulations, and the reference value of [58]. In every case, the transition is continuous, proving the robustness of the HANDOFF.

In Fig. 11 we plot the accretion rate at the horizon ( $\sim 2.65$  km) for BNS\_SmallRout\_t0, BNS\_SmallRout\_t1 and BNS\_LargeRout\_t1. The plot demonstrates the robustness of the HANDOFF in the following senses. First, the initial values of the accretion rate for the later transitions at  $t_1$ , BNS\_SmallRout\_t1 and BNS\_LargeRout\_t1, match the accretion rate of BNS\_SmallRout\_t0 at time  $t_1$ , proving both that the HANDOFF does not introduce unphysical transients and that the evolution of BNS\_SmallRout\_t0 follows the continuing run in ILLINOISGRMHD. Second, the plot shows that the extrapolation of primitives and spacetime metric for BNS\_LargeRout\_t1 does not lead to unphysical results but matches the results from runs where extrapolation was not needed. Third, the accretion rate approximates to the reference value  $\sim 0.2 M_{\odot} s^{-1}$  [58].

In Fig. 12 (*top*) we plot the evolution of the magnetic energy for our post-merger simulations, decomposed into toroidal and poloidal components (see Eqs. 23-25), integrated out of the BH horizon. For our fiducial run, BNS\_LargeRout\_t1, we find  $E_{\text{mag}} \sim 10^{49}$  erg, with a dominant toroidal component. Our results in this respect are not comparable with the reference simulations of Refs. [58] or [66], because their initial magnetic field was weaker than ours by three orders of magnitude. Instead, we consider the simulation H4B15d150 of Ref. [61], that has an initial field of similar strength, makes use of comparable resolution during the merger, and, though it uses a different EoS, the HMNS collapses to a BH rather promptly. With respect to this simulation, we find a consistent order of magnitude for  $E_{\text{mag}}$ . Further, the

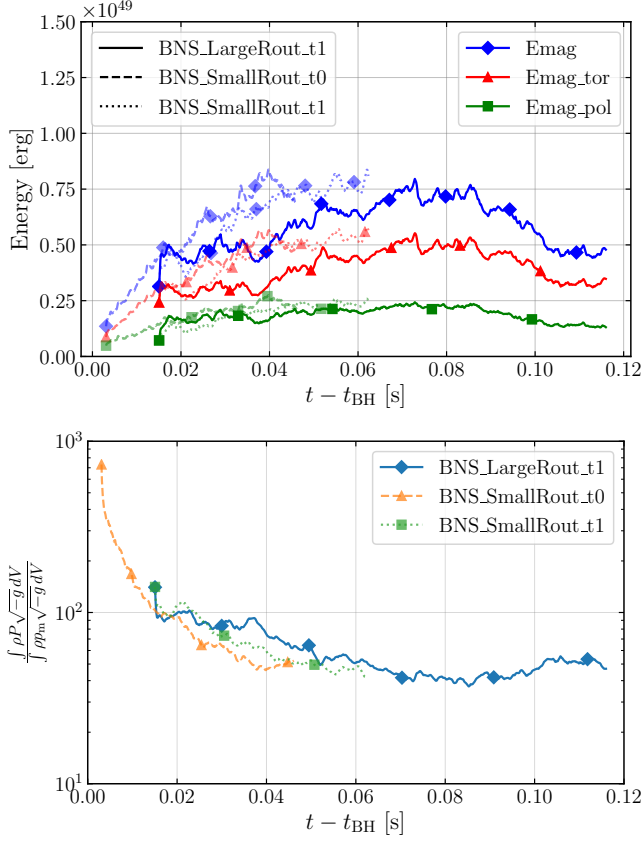


FIG. 12. *Top*: Magnetic energy of BNS post-merger runs (blue), decomposed into toroidal (red) and poloidal (green) components. *Bottom*: Ratio of the  $\rho$ -weighted integrals of thermal and magnetic pressure, as a measure of the magnetization of the disk for BNS post-merger runs.

dominance of the toroidal component after merger is a well-known result from the literature [see, for instance, Ref. 66]. From these results, we conclude the HANDOFF captures the correct strength and topology of the magnetic field after merger. In Appendix C we present resolution diagnostics that demonstrate that the MRI is properly resolved during our runs.

To better understand the effect of transitioning between codes on the magnetization of the disk, in Fig. 12 (*top*) we also plot the curves for the earlier transition `BNS_SmallRout_t0`, and for `BNS_SmallRout_t1`. For every simulation, we notice the magnetic energy grows initially, as expected from magnetic winding and the MRI, but we notice that the curves for the later transitions, `BNS_SmallRout_t1` and `BNS_LargeRout_t1`, do not match the curves of `BNS_SmallRout_t0` at  $t_1$ . Instead, the later transitions are initialized to a lower value than `BNS_SmallRout_t0` at  $t_1$ , indicating that the magnetic growth is faster in HARM3D than in ILLINOISGRMHD, plausibly because the grid of the former has higher resolution and spherical topology, better resolving the magnetic winding effects and the MRI. In fact, we notice that the magnetic energy of the later transitions have a very

steep initial growth, until they catch up with the evolved values in `BNS_SmallRout_t0`.

To measure the dynamical relevance of the magnetic field in the disk, in Fig. 12 (*bottom*) we plot the evolution of the ratio of the  $\rho$ -weighted integrals of thermal and magnetic pressure (see Eq. (21)). We find that the dynamical relevance of the field grows in time, until saturation at  $\sim 50$ . As a comparison, the FM evolved in the last section, has  $\sim 30$  for this ratio, at  $t = 9000M$ .

In Fig. 13 we show a poloidal plot of the magnetization  $b^2/\rho$  (*left*), and of the radial velocity of the fluid (*right*) with magnetic field lines (*green arrows*), at the end of our fiducial run. Although the magnetization of the disk and the spin of the BH are rather high, we notice that the material in the funnel is not magnetically dominated and a jet has not developed. This is in agreement with results from [66]. Several reasons might help to explain the absence of magnetic outflows: accretion of predominantly toroidal fields disfavours the formation of large-scale magnetic fields at the funnel and its subsequent amplification [see, for instance, 114–116]; while a long-lived NS remnant can build a strong helical field at the funnel, prompt collapse prevents this scenario [72, 74]; we ignore the drag from neutrino winds, which might help lower the degree of baryon pollution in the polar regions [117]. Still, in Fig. 13 (*right*) we notice a moderate ordering of the magnetic field lines at the funnel, plausibly stretched by the inflowing material. A mildly relativistic jet might arise in the longer-term [see 74, and refs. therein]. While the magnetic outflows are suppressed, Fig. 13 (*right*) shows outgoing parcels of fluid, or *winds*, at the boundary of the funnel and the disk [114].

Finally, we demonstrate the physical validity of the extrapolated metric. In Fig. 14 we plot the radial velocity  $v^r$  for `BNS_LargeRout_t1` and `BNS_SmallRout_t1`, averaged in  $\theta$  and  $\phi$ :

$$\langle v^r \rangle (r) = \frac{\int v^r \sqrt{-g} d\theta d\phi}{\int \sqrt{-g} d\theta d\phi}. \quad (26)$$

We plot  $\langle v^r \rangle (r)$  far from the BH, at the boundary of the ejecta with the numerical atmosphere, at three different times:  $t - t_{\text{BH}} = 0.015, 0.04, 0.089$  s (*left to right*). The *dotted-dashed* line in Fig. 14 represents the outer boundary of `BNS_SmallRout_t1` ( $\sim 4300$  km). First, we notice that in both runs the ejecta expand freely through the domain, showing the continuity of the handed-off transition. Next, we notice the curves for `BNS_LargeRout_t1` and `BNS_SmallRout_t1` at  $t - t_{\text{BH}} = 0.015, 0.04$  s are qualitatively the same. Since `BNS_LargeRout_t1` makes use of the extrapolated metric, and `BNS_SmallRout_t1` makes use of the interpolated numerical metric, we conclude these metrics are physically equivalent. We include a later curve for `BNS_LargeRout_t1` at  $t - t_{\text{BH}} = 0.089$  s to show that the HANDOFF allows for the expansion of the ejecta even further out than the outer boundary of the merger simulation ( $\sim 5700$  km). We do not include this curve for `BNS_SmallRout_t1` because we did not evolve this run for long enough.

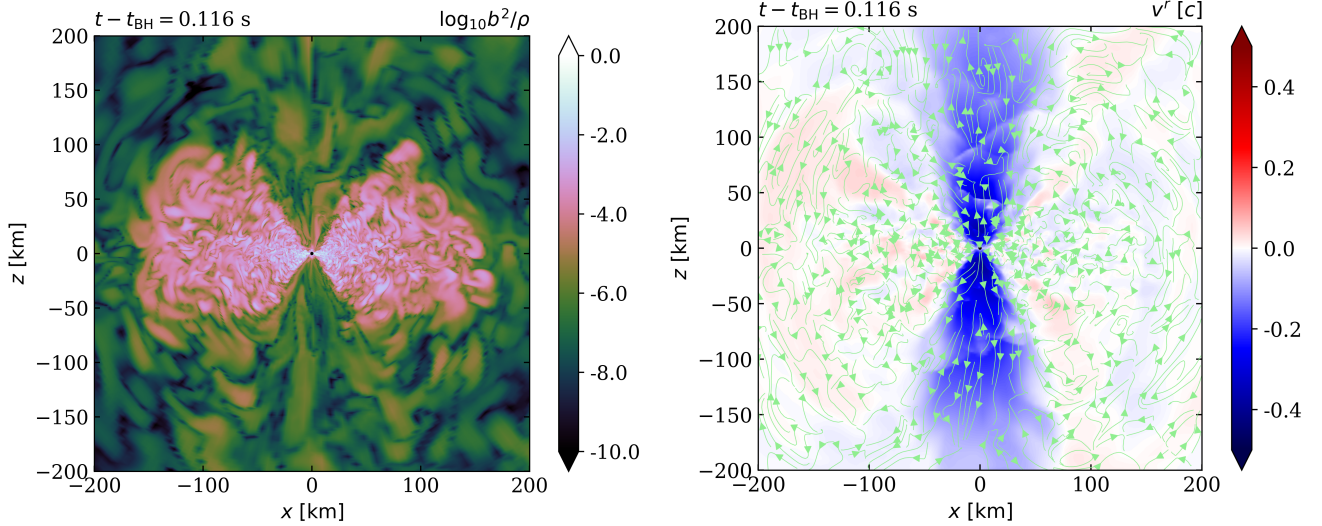


FIG. 13. *Left:* Magnetization  $b^2/\rho$  at the end of `BNS_LargeRout_t1`. We notice that, although the disk is fairly magnetized, the funnel is not magnetically dominated. *Right:* Radial velocity  $v^r$  and magnetic field lines (green) at the end of `BNS_LargeRout_t1`. We notice the absence of outflows at the funnel, and that magnetic field lines are poorly ordered.

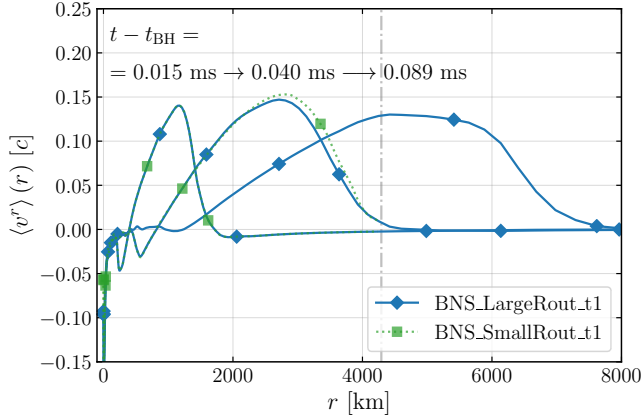


FIG. 14. Radial velocity of the ejecta, averaged in  $\theta$  and  $\phi$ , at three different times  $t - t_{BH} = 0.015, 0.04, 0.089$  ms (*left to right*). The grey, dotted-dashed line represents the outer boundary of `BNS_SmallRout_t1`. We notice that the ejecta expand freely through the domain, indicating that the numerical atmosphere and extrapolated metric (`BNS_LargeRout_t1`) introduced in the HANOFF are physically valid. The qualitative agreement between the curves of `BNS_SmallRout_t1` and `BNS_LargeRout_t1` reflects the near equivalence between the interpolated numerical metric and extrapolated metric.

## V. SUMMARY AND DISCUSSION

We presented the tools to transition a GRMHD simulation between two numerical codes, ILLINOISGRMHD and HARM3D, that make use of numerical grids with different resolutions and topologies. Moreover, we presented techniques to extrapolate the spacetime metric and MHD primitives to arbitrarily large radii, allowing

us to extend the numerical domain of the destination grid. This set of methods, enclosed under the name of the HANOFF, are particularly interesting for transitioning the outcomes of BNS or BH-NS mergers to a grid adapted to the geometry and requirements of the post-merger. In Appendix A we give the implementation details of this grid.

We validated the HANOFF with the well-known case of a magnetized torus around a rotating BH. We applied the HANOFF at different stages of the accretion process and confirmed the package successfully captures the state of the plasma and spacetime metric and transforms them to a general grid.

We applied the HANOFF to a BNS post-merger, after the BH had formed. We modeled matter as a magnetized ideal fluid with adiabatic index  $\Gamma = 2$ . To test the reliability of the HANOFF, we applied it at different times and to different destination grids. Our fiducial simulation, `BNS_LargeRout_t1`, starts from ID provided by the HANOFF at  $t - t_{BH} = 0.015$ s, makes use of the large grid described in Appendix A, and lasts for  $\sim 0.1$ s. Since the destination grid is larger than the initial grid for the merger, we needed to extrapolate the MHD primitives and spacetime metric to the complementary cells. After a careful analysis, we demonstrated our results from the HANOFF are independent of the time of transition, and of the destination grid. Furthermore, we showed these results are in agreement with reference simulations in the literature.

We conclude that HANOFF enables one to perform long-term, highly accurate and coordinate-optimized simulations of BNS post-mergers, using as initial data the end of a BNS inspiral/merger GRMHD simulation performed in full numerical relativity. Future work will focus on improving our models for the matter fields during the

merger, adopting finite-temperature and tabulated EoS and taking neutrino effects into account. Next, we will extend the HANDOFF to transition these realistic simulations to the modern code HARM3D+NUC [81].

## ACKNOWLEDGMENTS

This work was primarily funded through NASA award TCAN-80NSSC18K1488. Z.B.E. and L.R.W. gratefully acknowledge support from NSF awards PHY-1806596, PHY-2110352, OAC-2004311, as well as NASA award ISFM-80NSSC18K0538. R.O.S. is supported by NSF awards PHY-2012057, PHY-1912632 and AST-1909534. B.J.K. is supported by NASA under award number 80GSFC21M0002. A.M-B is supported by the UCMEXUS-CONACYT Doctoral Fellowship, and NASA through the NASA Hubble Fellowship grant HST-HF2-51487.001-A awarded by the Space Telescope Science Institute, which is operated by the Association of Universities for Research in Astronomy, Inc., for NASA, under contract NAS5-26555. V.M. is supported by the Exascale Computing Project (17-SC-20-SC), a collaborative effort of the U.S. Department of Energy (DOE) Office of Science and the National Nuclear Security Administration. Work at Oak Ridge National Laboratory is supported under contract DE-AC05-00OR22725 with the U.S. Department of Energy.

## Appendix A: Design of Post-merger Grid

The distorted spherical grid we often use in HARM3D, one that uses a uniform spacing in  $\log(r)$  and is concentrated in the poloidal direction near the equator, is not particularly well-suited for long-term evolutions of ejecta launched closer to the equator *and* relatively narrow jets along the poles. In order to resolve the jet at large distances and keep the number of poloidal cells fixed, we must increase  $\Delta\theta$  in the equator and decrease it near the poles as  $r$  grows. Using larger  $\Delta\theta$  at the smallest radii also allows us to use larger time steps, as they are set by the smallest cell-crossing time of the fastest MHD wave in the domain, which is usually determined by the innermost azimuthal extent at the poles,  $\simeq r_{\text{in}} (\Delta\theta/2) \Delta\phi$ , where  $r_{\text{in}}$  is the innermost radial coordinate on the grid. This means that our conventional grid is adequate at smaller radii, but we must transition to one that is more focused along the poles at larger radii.

Since the goal is to capture the ejected material out to  $\mathcal{O}(1s)$  of time or  $\mathcal{O}(1 \text{ light-second}) \sim \mathcal{O}(10^5 GM_{\text{BH}}/c^2)$  of distance, our typical  $\log(r)$  grid would require so many grid points it would be computationally prohibitive. Since the ejected material is expected to be nearly ballistic beyond  $r \simeq 10^3 M_{\text{BH}}$ , increasing  $\Delta r(r)$  in a hyper-exponential way provides an effective solution at covering

large distances with fewer cells:

$$r(x^{(1)}) = r_0 + (r_{\text{in}} - r_0) \times \exp \left[ c_1 \left( x^{(1)}/x_{\text{he}} \right) + c_2 \left( x^{(1)}/x_{\text{he}} \right)^n \right] , \quad (\text{A1})$$

where the coefficients in the exponent ensure that  $r(0) = r_{\text{in}}$ ,  $r(x_{\text{he}}) = r_{\text{he}}$ ,  $r(1) = r_{\text{out}}$  ( $r_{\text{out}}$  is the outermost radial coordinate):

$$c_1 = \frac{d_1 - d_2 x_{\text{he}}^n}{1 - x_{\text{he}}^{n-1}} , \quad c_2 = \frac{d_2 x_{\text{he}}^n - d_1 x_{\text{he}}^{n-1}}{1 - x_{\text{he}}^{n-1}} , \quad (\text{A2})$$

and

$$d_1 = \ln \left( \frac{r_{\text{he}} - r_{\text{in}}}{r_{\text{in}} - r_0} \right) , \quad d_2 = \ln \left( \frac{r_{\text{out}} - r_{\text{in}}}{r_{\text{in}} - r_0} \right) . \quad (\text{A3})$$

For the run `BNS_LargeRout_t1` we use  $n = 10$ ,  $r_0 = 0$ ,  $r_{\text{in}} = 1.31 M_{\odot}$ ,  $r_{\text{he}} = 10^4 M_{\odot}$ ,  $r_{\text{out}} = 7.2 \times 10^4 M_{\odot}$ ,  $dx^{(1)} = 1/1024$ , and  $0 \leq x^{(1)} \leq 1$ .

The poloidal discretization joins two regions: an inner one with cells focused near the equator and an outer region with more cells near the poles. The two regions are smoothly and continuously connected through use of a transition function, similar to the strategy used in our “dual fisheye” grids [102]. The poloidal coordinate in terms of the numerical coordinate  $x^{(2)}$  is:

$$\theta(x^{(2)}) = \pi \left\{ x^{(2)} - a_2 \left[ \mathcal{T}(x^{(2)}) - \mathcal{T}(1/2) - (x^{(2)} - 1/2) (\mathcal{T}(1) - \mathcal{T}(0)) \right] \right\} , \quad (\text{A4})$$

where  $\mathcal{T}(x)$  is the integral of the approximate boxcar function from [102]:

$$\mathcal{T}(x^{(2)}) \equiv \frac{1}{2} \left[ \Sigma(x^{(2)} - 1/2 + \delta_2) - \Sigma(x^{(2)} - 1/2 - \delta_2) \right] . \quad (\text{A5})$$

and

$$\Sigma(x) \equiv \frac{1}{h_2} \ln \cosh(h_2 x) . \quad (\text{A6})$$

Here,  $h_2$  controls the steepness of the transition, and  $\delta_2$  controls the fraction of cells that are in the equatorial portion of the poloidal grid. We use  $h_2 = 20$ ,  $\delta_2 = 0.3$ ,  $dx^{(2)} = 1/200$ , and  $0 \leq x^{(2)} \leq 1$ .

The transition between the inner and outer regions is handled by changing the amplitude of the grid distortion,  $a_2$ , w.r.t.  $r$ :

$$a_2 = a_2(r) \equiv a_{21} f(r, r_j, h_j) + [1 - f(r, r_j, h_j)] a_{22} , \quad (\text{A7})$$

where the transition function is

$$f(r, r_j, h_j) \equiv \frac{1}{2} \{ 1 + \tanh[h_j(r - r_j)] \} . \quad (\text{A8})$$

The two amplitudes,  $a_{21}$  and  $a_{22}$ , are set by different criteria. The amplitude for the inner portion is set so

that the spacing near the equator is such that the number of cells per vertical disk scale height,  $N_{H/r}$ , is equal to the 32 cells recommended to adequately resolve the MRI [118]:

$$a_{21} = \frac{1 - N_2 (H/r) / (\pi N_{H/r})}{1 - 2\delta_2} , \quad (\text{A9})$$

where  $N_2$  is the number of cell extents in the  $x^{(2)}$  direction. The outer amplitude is set so that the poloidal spacing near the poles follow the parabolic flow contours often found in the jets of GRMHD simulations [119]:  $z = R^{n_1}$ , where  $R \equiv r \sin \theta$  is the cylindrical radius, and  $1 < n_1 \lesssim 2.67$  for general outflows. Using the small angle approximation,  $\theta \simeq r^{n_j}$ , where  $n_j \equiv (1/n_1 - 1)$ . The funnel wall shape arising in GRMHD simulations with spinning black holes closely follows the curve with  $n_1 \simeq 3/2$  or  $n_j \simeq -1/3$  [119], and is the value used here. The amplitude,  $a_{22}$ , must vary with radius such that  $d\theta_j$ , the approximately  $x^{(2)}$ -independent spacing local to the jet, follows these contours at  $r > r_j$ , where  $r_j$  is the radius at which we specify this transition occurs. At  $r = r_j$ , we set  $d\theta_j$  to be 90% of what it would be if the grid was uniform in  $\theta$ . The amplitude is finally calculated using this  $r$ -dependent  $d\theta_j$ :

$$a_{22} = -\frac{1 - N_2 d\theta_j(r)/\pi}{2\delta_2} , \quad (\text{A10})$$

where  $d\theta_j(r) = (0.9\pi/N_2) (r/r_j)^{n_j}$ ,  $n_j = -1/3$ , and  $r_j = 300M_\odot$ .

The azimuthal grid spacing for the new grid remains uniform, with  $\phi \in [0, 2\pi]$  and  $d\phi = 2\pi/N_3$ , where  $N_3$  is the number of cells in the azimuthal extent.

In Fig. 5 (right) we plot the cell-lengths of this grid, as a function of radii and  $\theta \in (0, \pi)$ . Regarding  $\Delta r$ , we notice the transition of its slope from exponential to hyper-exponential at  $r \sim 10^3$  km. Although  $\Delta\phi$  is uniform, the cell-length  $r \sin \theta \Delta\phi$  grows with  $r$  because of its explicit radial dependence, and spans different resolutions at a given radius because of the different values of  $\theta \in (0, \pi)$ . Finally,  $r\Delta\theta$  also grows with  $r$  because of its explicit radial dependence, and spans different values at a given radius because, as described above,  $\Delta\theta$  is not uniform but focuses on the equator at small radii, and on the axis at larger radii. We notice this transition at  $r \sim 10^3$  km.

## Appendix B: Boundary conditions at the axis

Previous simulations of accretion disks in HARM3D excise a portion of the domain around the polar axis [see, for instance, 80, 108, 120]. In these simulations, the polar coordinate  $\theta$  is restricted to an interval  $(\theta_c, \pi - \theta_c)$ , where  $\theta_c > 0$  is the extent of the *cutout* in  $\theta$  from the axis. This is convenient for two reasons: First, the coordinate singularity at the axis is excised from the domain. Second, the innermost azimuthal extent at the poles is

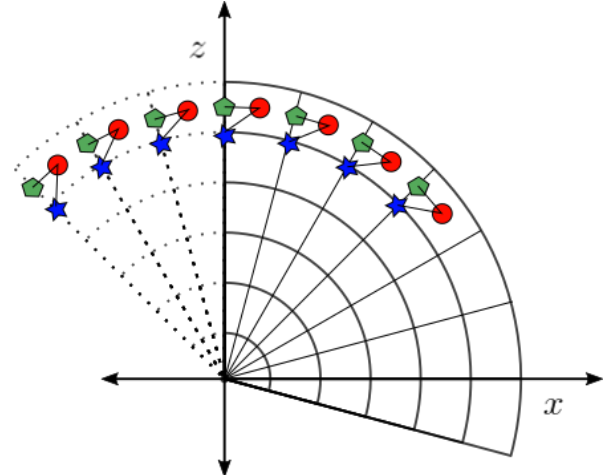


FIG. 15. Sketch of grid cells next to the positive  $z$ -axis. Red circles represent the positions of the cell-centers, green polygons represent the position of the lower  $\theta$ -face of each cell, and blue stars represent the lower corners. Dotted cells represent ghost cells. The cell-center of these ghost cells are mapped to the cell-center of physical cells across the axis. The lower faces and corners of the ghost cells, however, are shifted by  $+\Delta\theta$  and map to the upper-face of the corresponding physical cells.

increased from  $r_{\text{in}} \sin(\Delta\theta/2)\Delta\phi$  to  $r_{\text{in}} \sin(\theta_c + \Delta\theta/2)\Delta\phi$  and, since the time step in spherical coordinates is restricted to the cell-crossing time of this extent, the time step is increased accordingly. However, cutting out the domain has its drawbacks: The simulation lacks a portion of the the funnel region and therefore of the magnetic outflows, and even the rest of the funnel might be affected by the boundary conditions imposed at the cutout, which are usually reflective or outflow.

These drawbacks are not severe in previous applications, where the funnel is mostly evacuated and the magnetic outflows expand through the numerical atmosphere, but that is not the case for a BNS post-merger. In the latter, the funnel is baryon polluted, with a complex magnetic field structure, and the magnetic outflows propagate through the dynamical ejecta creating a complex jet-cocoon system that eventually breaks-out from the debris. A cutout in  $\theta$  would prohibit the appropriate modelling of these phenomena. For this reason, we remove the cutout and implement appropriate boundary conditions at the polar axis, as we describe below.

Formally, the cutout is still present to avoid the coordinate singularity at the axis, but it is reduced to a small value. Specifically, the cell-centered coordinates of the cells next to the positive [negative]  $z$ -axis have coordinates  $(r, \Delta\theta/2 + \theta_c, \phi) [ (r, \pi - \Delta\theta/2 - \theta_c, \phi) ]$ , with  $\theta_c \sim 10^{-14}$ . The three ghost cells in  $\theta$  before [after] these cells are mapped to the physical coordinates across the axis, with cell-centered coordinates  $(r, \theta_c + j\Delta\theta + \Delta\theta/2 + \theta_c, \phi + \pi) [ (r, \pi - \theta_c - j\Delta\theta - \Delta\theta/2 - \theta_c, \phi + \pi) ]$ , with  $j = 0, 1, 2$ . In Fig. 15 we sketch the cell-centers of physical and ghost cells (*dashed*) around the positive  $z$ -axis

with *red circles*.

Although the cell-centers of the ghost cells in  $\theta$  match the cell-centers of physical cells across the axis, that is not the case for the lower corners and lower  $\theta$ -faces. The cell-corners and lower  $\theta$ -faces of the ghost cells are shifted by  $+\Delta\theta$ , so they stand at a cell-length distance from the corresponding cell positions at the boundary. In other words, the lower  $\theta$ -face of the ghost cells maps to the upper  $\theta$ -face of the physical cells across the axis. In Fig. 15 we sketch the positions of the lower  $\theta$ -faces for ghosts (*dashed*) and physical cells with *green polygons*, and the corners with *blue stars*. This is important, for instance, when calculating finite differences across the axis for the spacetime connections, or for the curl of  $A_\mu$ .

Having set the coordinates of the ghost cells in  $\theta$ , we evaluate the spacetime metric at these cells, and multiply its components  $g_{\mu\nu}$  by parity factors that ensure continuity across the axis. In particular, we follow Refs. [78] (see Table 1 of that reference) and change the sign of  $g_{t\theta}, g_{r\theta}, g_{\phi\theta}$  and their symmetric permutations. The metric component  $g_{\phi\phi}$  tends to zero towards the axis, so we enforce  $g_{\phi\phi} = 1 \times 10^{-14}$  if this component takes a smaller value at the  $\theta$ -face and corners of the physical cells next to the axis. We fill the ghost cells with MHD primitives from the matching physical cells, and take parity factors into account by changing the sign of the tensor components  $B^\theta, v^\theta$  [78]. We use the geometry and primitives in these ghost regions as boundary conditions to evolve the conserved variables in the physical cells next to the axis. Subsequently, the MHD primitives in the ghost cells are updated after each time step with the evolved values at the matching physical cells, and multiplied by the corresponding parity factors.

The evolution of the magnetic field requires further care. In the `FluxCT` algorithm [89], the electric field  $\mathbf{E}$  is calculated at the cell-edges, and the extent or definition of those edges is singular for cells next to the axis. As first described by Refs. [121] (see the supplementary material of that reference), we find that a non-zero value of  $E_\phi$  at the axis gives raise to an artificial growth of the magnetic flux in the radial direction. We apply the same techniques of Ref. [121] to circumvent this problem. Since the extent of the cell-edge in  $\phi$  is zero at the axis, we set the electric field component  $E_\phi$  to zero in those cells. Further, since the cell-edge in  $r$  is the same for every cell around the axis at a given height  $z$ , we set  $E_r$  to a unique value in these cells. This value results from the  $\phi$ -average of  $E_r$  around the axis at height  $z$ .

### Appendix C: Resolution Diagnostics

In this appendix we calculate resolution diagnostics to demonstrate the convergence of the MRI-driven turbu-

lence in the post-merger disk. We follow the analyses of Refs. [76, 108, 122, 123].

We start by calculating the number of cells within the linear MRI wavelength, or quality factors:

$$Q^{(i)} = \frac{2\pi |b^{(i)}|}{\Delta x^{(i)} \Omega_K(r) \sqrt{\rho h + 2p_m}}. \quad (C1)$$

We multiply the latter by  $\rho$  to focus on the disk, and average over the polar direction:

$$\langle Q^{(i)} \rangle_\rho (r, \phi) = \frac{\int_0^1 Q^{(i)} \rho \sqrt{g^r} dx^{(2)}}{\int_0^1 \rho \sqrt{g^r} dx^{(2)}}. \quad (C2)$$

In Fig. 16 we plot these quantities at the end of `BNS_LargeRout_t1`, and notice they satisfy  $\langle Q^{(2)} \rangle_\rho > 10$  and  $\langle Q^{(3)} \rangle_\rho > 20$ , the conditions for converged MRI behavior from resolution studies.

We also calculate non-linear diagnostics: The weighted ratio of the Maxwell stress to the magnetic pressure

$$\langle \alpha_{\text{mag}} \rangle_\rho = \frac{\int \alpha_{\text{mag}} \rho \sqrt{g} dV}{\int \rho \sqrt{g} dV}, \quad \alpha_{\text{mag}} = \frac{2\sqrt{b_r b^r} \sqrt{b_\phi b^\phi}}{b^2}, \quad (C3)$$

and the weighted ratio of energies between these components

$$\mathcal{R} = \frac{\int B_r B^r \rho \sqrt{-g} dV}{\int B_\phi B^\phi \rho \sqrt{-g} dV}. \quad (C4)$$

In Fig. 17 we plot these quantities as a function of time. We find  $\alpha_{\text{mag}}$  becomes approximately constant, as expected from the correlation induced on  $b^r$  and  $b^\phi$  by the MRI, and converges to  $\sim 0.4$ , the saturation value of shearing-box simulations of Ref. [122]. On the other hand, we find  $\mathcal{R} \sim 0.3 > 0.2$ , satisfying the criteria of Ref. [123]. From this plot we also notice that the later transitions, `BNS_SmallRout_t1` and `BNS_LargeRout_t1`, are initialized to a smaller value than `BNS_SmallRout_t0` at such time, and then they rapidly catch up with the convergent value. This suggests the MRI was not properly resolved in `ILLINOISGRMHD`, proving the need for the transition to a higher-resolution grid. We conclude the MRI is well-resolved in the run `BNS_LargeRout_t1` that makes use of the grid described in Appendix A.

[1] R. Abbott *et al.* (LIGO Scientific Collaboration and Virgo Collaboration), Gwtc-2: Compact binary coales-

ences observed by ligo and virgo during the first half

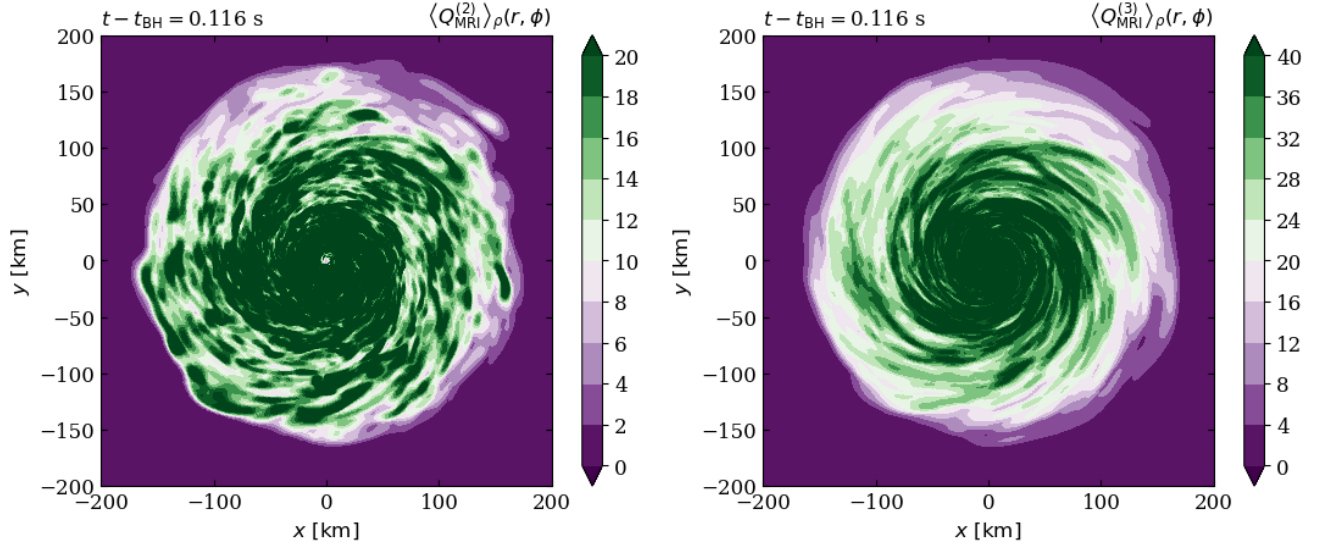


FIG. 16. Quality factors of MRI resolution, weighted by  $\rho$  and averaged in  $\theta$ . We emphasize they satisfy  $\langle Q_{\text{MRI}}^{(2)} \rangle_{\rho} > 10$  (left) and  $\langle Q_{\text{MRI}}^{(3)} \rangle_{\rho} > 20$  (right), adequately resolving the MRI wavelength.

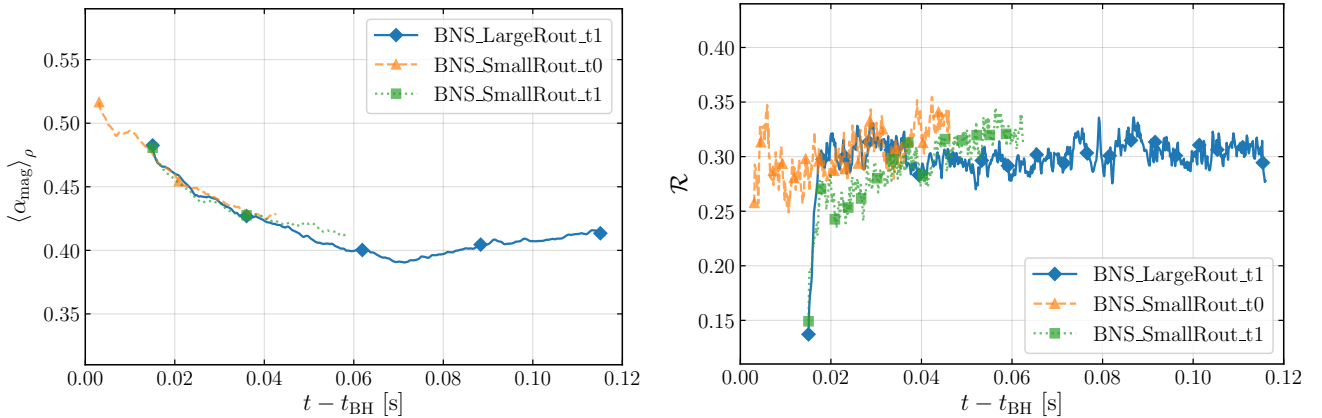


FIG. 17. Non-linear diagnostics of MRI resolution  $\alpha_{\text{mag}}$  (left) and  $\mathcal{R}$  (right) (see Eqs. C3 and C4). They converge to  $\sim 0.4$  and  $\sim 0.3$ , respectively, implying proper resolution of the MRI modes [122, 123].

of the third observing run, Phys. Rev. X **11**, 021053 (2021).

[2] D. A. Coulter, R. J. Foley, C. D. Kilpatrick, M. R. Drout, A. L. Piro, B. J. Shappee, M. R. Siebert, J. D. Simon, N. Ulloa, D. Kasen, B. F. Madore, A. Murguia-Berthier, Y.-C. Pan, J. X. Prochaska, E. Ramirez-Ruiz, A. Rest, and C. Rojas-Bravo, Swope supernova survey 2017a (sss17a), the optical counterpart to a gravitational wave source, Science **358**, 1556 (2017).

[3] B. P. Abbott *et al.* (LIGO Scientific Collaboration and Virgo Collaboration), Gw170817: Observation of gravitational waves from a binary neutron star inspiral, Phys. Rev. Lett. **119**, 161101 (2017).

[4] B. P. Abbott *et al.* (LIGO Scientific Collaboration and Virgo Collaboration), Properties of the binary neutron star merger gw170817, Phys. Rev. X **9**, 011001 (2019).

[5] A. Goldstein *et al.*, An ordinary short gamma-ray burst with extraordinary implications: Fermi -GBM detection of GRB 170817a, The Astrophysical Journal **848**, L14 (2017).

[6] D. Eichler, M. Livio, T. Piran, and D. N. Schramm, Nucleosynthesis, neutrino bursts and  $\gamma$ -rays from coalescing neutron stars, Nature **340**, 126 (1989).

[7] R. Narayan, B. Paczynski, and T. Piran, Gamma-Ray Bursts as the Death Throes of Massive Binary Stars, Astrophysical Journal Letters **395**, L83 (1992).

[8] W. H. Lee and E. Ramirez-Ruiz, The progenitors of short gamma-ray bursts, New Journal of Physics **9**, 17 (2007).

[9] E. Nakar, Short-hard gamma-ray bursts, Physics Reports **442**, 166 (2007), the Hans Bethe Centennial Volume 1906-2006.

[10] E. Berger, Short-duration gamma-ray bursts, Annual Review of Astronomy and Astrophysics **52**, 43 (2014).

[11] O. Gottlieb, E. Nakar, and T. Piran, The cocoon emission - an electromagnetic counterpart to gravitational waves from neutron star mergers, *Monthly Notices of the Royal Astronomical Society* **473**, 576 (2018).

[12] D. Lazzati, R. Perna, B. J. Morsony, D. Lopez-Camara, M. Cantiello, R. Ciolfi, B. Giacomazzo, and J. C. Workman, Late Time Afterglow Observations Reveal a Collimated Relativistic Jet in the Ejecta of the Binary Neutron Star Merger GW170817, *Phys. Rev. Lett.* **120**, 241103 (2018).

[13] O. Bromberg, A. Tchekhovskoy, O. Gottlieb, E. Nakar, and T. Piran, The  $\gamma$ -rays that accompanied GW170817 and the observational signature of a magnetic jet breaking out of NS merger ejecta, *Monthly Notices of the Royal Astronomical Society* **475**, 2971 (2018).

[14] O. Gottlieb, E. Nakar, T. Piran, and K. Hotokezaka, A cocoon shock breakout as the origin of the gamma-ray emission in GW170817, *Monthly Notices of the Royal Astronomical Society* **479**, 588 (2018).

[15] M. Soares-Santos *et al.*, The electromagnetic counterpart of the binary neutron star merger LIGO/virgo GW170817. i. discovery of the optical counterpart using the dark energy camera, *The Astrophysical Journal* **848**, L16 (2017).

[16] M. R. Drout *et al.*, Light curves of the neutron star merger gw170817/sss17a: Implications for r-process nucleosynthesis, *Science* **358**, 1570 (2017).

[17] P. S. Cowperthwaite *et al.*, The electromagnetic counterpart of the binary neutron star merger LIGO/virgo GW170817. II. UV, optical, and near-infrared light curves and comparison to kilonova models, *The Astrophysical Journal* **848**, L17 (2017).

[18] M. Nicholl *et al.*, The electromagnetic counterpart of the binary neutron star merger LIGO/virgo GW170817. III. optical and UV spectra of a blue kilonova from fast polar ejecta, *The Astrophysical Journal* **848**, L18 (2017).

[19] R. Chornock *et al.*, The electromagnetic counterpart of the binary neutron star merger LIGO/virgo GW170817. IV. detection of near-infrared signatures of r-process nucleosynthesis with gemini-south, *The Astrophysical Journal* **848**, L19 (2017).

[20] E. Pian *et al.*, Spectroscopic identification of r-process nucleosynthesis in a double neutron-star merger, *Nature (London)* **551**, 67 (2017).

[21] L.-X. Li and B. Paczyński, Transient events from neutron star mergers, *The Astrophysical Journal* **507**, L59 (1998).

[22] B. D. Metzger, G. Martínez-Pinedo, S. Darbha, E. Quataert, A. Arcones, D. Kasen, R. Thomas, P. Nugent, I. V. Panov, and N. T. Zinner, Electromagnetic counterparts of compact object mergers powered by the radioactive decay of r-process nuclei, *Monthly Notices of the Royal Astronomical Society* **406**, 2650 (2010).

[23] L. F. Roberts, D. Kasen, W. H. Lee, and E. Ramirez-Ruiz, Electromagnetic transients powered by nuclear decay in the tidal tails of coalescing compact binaries, *The Astrophysical Journal* **736**, L21 (2011).

[24] S. Goriely, A. Bauswein, and H.-T. Janka, r-process nucleosynthesis in dynamically ejected matter of neutron star mergers, *The Astrophysical Journal* **738**, L32 (2011).

[25] B. D. Metzger and E. Berger, What is the most promising electromagnetic counterpart of a neutron star binary merger?, *The Astrophysical Journal* **746**, 48 (2012).

[26] C. D. Kilpatrick *et al.*, Electromagnetic evidence that sss17a is the result of a binary neutron star merger, *Science* **358**, 1583 (2017).

[27] G. Hallinan *et al.*, A radio counterpart to a neutron star merger, *Science* **358**, 1579 (2017).

[28] E. Troja *et al.*, The x-ray counterpart to the gravitational-wave event gw170817, *Nature* **551**, 71 (2017).

[29] K. P. Mooley *et al.*, A mildly relativistic wide-angle outflow in the neutron-star merger event gw170817, *Nature* **554**, 207 (2018).

[30] R. Margutti *et al.*, The binary neutron star event LIGO/virgo GW170817 160 days after merger: Synchrotron emission across the electromagnetic spectrum, *The Astrophysical Journal* **856**, L18 (2018).

[31] E. Troja, L. Piro, G. Ryan, H. van Eerten, R. Ricci, M. H. Wieringa, S. Lotti, T. Sakamoto, and S. B. Cenko, The outflow structure of GW170817 from late-time broad-band observations, *Monthly Notices of the Royal Astronomical Society: Letters* **478**, L18 (2018).

[32] K. P. Mooley, D. A. Frail, D. Dobie, E. Lenc, A. Corsi, K. De, A. J. Nayana, S. Makhathini, I. Heywood, T. Murphy, D. L. Kaplan, P. Chandra, O. Smirnov, E. Nakar, G. Hallinan, F. Camilo, R. Fender, S. Goedhart, P. Groot, M. M. Kasliwal, S. R. Kulkarni, and P. A. Woudt, A strong jet signature in the late-time light curve of GW170817, *The Astrophysical Journal* **868**, L11 (2018).

[33] K. P. Mooley, A. T. Deller, O. Gottlieb, E. Nakar, G. Hallinan, S. Bourke, D. A. Frail, A. Horesh, A. Corsi, and K. Hotokezaka, Superluminal motion of a relativistic jet in the neutron-star merger gw170817, *Nature* **561**, 355 (2018).

[34] M. M. Kasliwal *et al.*, Illuminating gravitational waves: A concordant picture of photons from a neutron star merger, *Science* **358**, 1559 (2017).

[35] G. Ghirlanda *et al.*, Compact radio emission indicates a structured jet was produced by a binary neutron star merger, *Science* **363**, 968 (2019).

[36] L. Baiotti and L. Rezzolla, Binary neutron star mergers: a review of einstein's richest laboratory, *Reports on Progress in Physics* **80**, 096901 (2017).

[37] M. Shibata and K. Hotokezaka, Merger and mass ejection of neutron star binaries, *Annual Review of Nuclear and Particle Science* **69**, 41 (2019).

[38] R. Ciolfi, Binary neutron star mergers after GW170817, *Frontiers in Astronomy and Space Sciences* **7**, 27 (2020).

[39] N. Sarin and P. D. Lasky, The evolution of binary neutron star post-merger remnants: a review, *General Relativity and Gravitation* **53**, 59 (2021).

[40] T. Dietrich, T. Hinderer, and A. Samajdar, Interpreting binary neutron star mergers: describing the binary neutron star dynamics, modelling gravitational waveforms, and analyzing detections, *General Relativity and Gravitation* **53**, 27 (2021).

[41] D. Radice, A. Perego, F. Zappa, and S. Bernuzzi, GW170817: Joint constraint on the neutron star equation of state from multimessenger observations, *The Astrophysical Journal* **852**, L29 (2018).

[42] C. A. Raithel, Constraints on the neutron star equation of state from gw170817, *The European Physical Journal A* **55**, 80 (2019).

[43] B. Margalit and B. D. Metzger, Constraining the maximum mass of neutron stars from multi-messenger obser-

vations of GW170817, *The Astrophysical Journal* **850**, L19 (2017).

[44] R. Ciolfi, Short gamma-ray burst central engines, *International Journal of Modern Physics D* **27**, 1842004 (2018).

[45] A. Murguia-Berthier, E. Ramirez-Ruiz, F. De Colle, A. Janiuk, S. Rosswog, and W. H. Lee, The Fate of the Merger Remnant in GW170817 and Its Imprint on the Jet Structure, *The Astrophysical Journal* **908**, 152 (2021).

[46] K. Hotokezaka, K. Kiuchi, K. Kyutoku, H. Okawa, Y.-i. Sekiguchi, M. Shibata, and K. Taniguchi, Mass ejection from the merger of binary neutron stars, *Phys. Rev. D* **87**, 024001 (2013).

[47] D. Radice, A. Perego, K. Hotokezaka, S. A. Fromm, S. Bernuzzi, and L. F. Roberts, Binary Neutron Star Mergers: Mass Ejection, Electromagnetic Counterparts, and Nucleosynthesis, *The Astrophysical Journal* **869**, 130 (2018).

[48] M. B. Davies, W. Benz, T. Piran, and F. K. Thielemann, Merging Neutron Stars. I. Initial Results for Coalescence of Noncorotating Systems, *The Astrophysical Journal* **431**, 742 (1994).

[49] S. Rosswog, M. Liebendörfer, F. K. Thielemann, M. B. Davies, W. Benz, and T. Piran, Mass ejection in neutron star mergers, *Astronomy and Astrophysics* **341**, 499 (1999).

[50] K.-i. Oohara and T. Nakamura, 3D General Relativistic Simulations of Coalescing Binary Neutron Stars, *Progress of Theoretical Physics Supplement* **136**, 270 (1999).

[51] M. Shibata and K. b. o. Uryū, Simulation of merging binary neutron stars in full general relativity:  $\Gamma = 2$  case, *Phys. Rev. D* **61**, 064001 (2000).

[52] M. Shibata, K. Taniguchi, and K. b. o. Uryū, Merger of binary neutron stars of unequal mass in full general relativity, *Phys. Rev. D* **68**, 084020 (2003).

[53] M. Anderson, E. W. Hirschmann, L. Lehner, S. L. Liebling, P. M. Motl, D. Neilsen, C. Palenzuela, and J. E. Tohline, Magnetized neutron-star mergers and gravitational-wave signals, *Phys. Rev. Lett.* **100**, 191101 (2008).

[54] L. Baiotti, B. Giacomazzo, and L. Rezzolla, Accurate evolutions of inspiralling neutron-star binaries: Prompt and delayed collapse to a black hole, *Phys. Rev. D* **78**, 084033 (2008).

[55] Y. T. Liu, S. L. Shapiro, Z. B. Etienne, and K. Taniguchi, General relativistic simulations of magnetized binary neutron star mergers, *Phys. Rev. D* **78**, 024012 (2008).

[56] B. Giacomazzo, L. Rezzolla, and L. Baiotti, Can magnetic fields be detected during the inspiral of binary neutron stars?, *Monthly Notices of the Royal Astronomical Society: Letters* **399**, L164 (2009).

[57] B. Giacomazzo, L. Rezzolla, and L. Baiotti, Accurate evolutions of inspiralling and magnetized neutron stars: Equal-mass binaries, *Phys. Rev. D* **83**, 044014 (2011), arXiv:1009.2468 [gr-qc].

[58] L. Rezzolla, B. Giacomazzo, L. Baiotti, J. Granot, C. Kouveliotou, and M. A. Aloy, The Missing Link: Merging Neutron Stars Naturally Produce Jet-like Structures and Can Power Short Gamma-ray Bursts, *Astrophysical Journal Letters* **732**, L6 (2011).

[59] C. Palenzuela, L. Lehner, M. Ponce, S. L. Liebling, M. Anderson, D. Neilsen, and P. Motl, Electromagnetic and gravitational outputs from binary-neutron-star coalescence, *Phys. Rev. Lett.* **111**, 061105 (2013).

[60] F. Foucart, E. O'Connor, L. Roberts, M. D. Duez, R. Haas, L. E. Kidder, C. D. Ott, H. P. Pfeiffer, M. A. Scheel, and B. Szilagyi, Post-merger evolution of a neutron star-black hole binary with neutrino transport, *Phys. Rev. D* **91**, 124021 (2015).

[61] K. Kiuchi, K. Kyutoku, Y. Sekiguchi, M. Shibata, and T. Wada, High resolution numerical-relativity simulations for the merger of binary magnetized neutron stars, *Phys. Rev. D* **90**, 041502 (2014).

[62] K. Kiuchi, P. Cerdá-Durán, K. Kyutoku, Y. Sekiguchi, and M. Shibata, Efficient magnetic-field amplification due to the Kelvin-Helmholtz instability in binary neutron star mergers, *Phys. Rev. D* **92**, 124034 (2015).

[63] A. Endrizzi, R. Ciolfi, B. Giacomazzo, W. Kastaun, and T. Kawamura, General relativistic magnetohydrodynamic simulations of binary neutron star mergers with the APR4 equation of state, *Classical and Quantum Gravity* **33**, 164001 (2016).

[64] M. Ruiz, R. N. Lang, V. Paschalidis, and S. L. Shapiro, Binary Neutron Star Mergers: A Jet Engine for Short Gamma-Ray Bursts, *Astrophysical Journal Letters* **824**, L6 (2016).

[65] R. Fernández, F. Foucart, D. Kasen, J. Lippuner, D. Desai, and L. F. Roberts, Dynamics, nucleosynthesis, and kilonova signature of black hole—neutron star merger ejecta, *Classical and Quantum Gravity* **34**, 154001 (2017).

[66] T. Kawamura, B. Giacomazzo, W. Kastaun, R. Ciolfi, A. Endrizzi, L. Baiotti, and R. Perna, Binary neutron star mergers and short gamma-ray bursts: Effects of magnetic field orientation, equation of state, and mass ratio, *Phys. Rev. D* **94**, 064012 (2016).

[67] R. Ciolfi, W. Kastaun, B. Giacomazzo, A. Endrizzi, D. M. Siegel, and R. Perna, General relativistic magnetohydrodynamic simulations of binary neutron star mergers forming a long-lived neutron star, *Phys. Rev. D* **95**, 063016 (2017).

[68] M. Ruiz and S. L. Shapiro, General relativistic magnetohydrodynamics simulations of prompt-collapse neutron star mergers: The absence of jets, *Phys. Rev. D* **96**, 084063 (2017).

[69] R. Ciolfi, W. Kastaun, J. V. Kalinani, and B. Giacomazzo, First 100 ms of a long-lived magnetized neutron star formed in a binary neutron star merger, *Phys. Rev. D* **100**, 023005 (2019).

[70] M. Ruiz, A. Tsokaros, V. Paschalidis, and S. L. Shapiro, Effects of spin on magnetized binary neutron star mergers and jet launching, *Phys. Rev. D* **99**, 084032 (2019).

[71] A. Tsokaros, M. Ruiz, V. Paschalidis, S. L. Shapiro, and K. Uryū, Effect of spin on the inspiral of binary neutron stars, *Phys. Rev. D* **100**, 024061 (2019).

[72] R. Ciolfi, Collimated outflows from long-lived binary neutron star merger remnants, *Monthly Notices of the Royal Astronomical Society* **495**, L66 (2020).

[73] M. Ruiz, A. Tsokaros, and S. L. Shapiro, Magnetohydrodynamic simulations of binary neutron star mergers in general relativity: Effects of magnetic field orientation on jet launching, *Phys. Rev. D* **101**, 064042 (2020).

[74] R. Ciolfi, The key role of magnetic fields in binary neutron star mergers, *General Relativity and Gravitation* **52**, 59 (2020).

[75] Some exceptions being [61, 62, 76, 117].

[76] K. Kiuchi, K. Kyutoku, Y. Sekiguchi, and M. Shibata, Global simulations of strongly magnetized remnant massive neutron stars formed in binary neutron star mergers, *Phys. Rev. D* **97**, 124039 (2018).

[77] R. Ciolfi and J. V. Kalinani, Magnetically Driven Baryon Winds from Binary Neutron Star Merger Remnants and the Blue Kilonova of 2017 August, *Astrophysical Journal Letters* **900**, L35 (2020).

[78] V. Mewes, Y. Zlochower, M. Campanelli, T. W. Baumgarte, Z. B. Etienne, F. G. L. Armengol, and F. Cipolletta, Numerical relativity in spherical coordinates: A new dynamical spacetime and general relativistic MHD evolution framework for the Einstein Toolkit, *Phys. Rev. D* **101**, 104007 (2020).

[79] Z. B. Etienne, V. Paschalidis, R. Haas, P. Mösta, and S. L. Shapiro, IllinoisGRMHD: an open-source, user-friendly GRMHD code for dynamical spacetimes, *Classical and Quantum Gravity* **32**, 175009 (2015).

[80] S. C. Noble, J. H. Krolik, and J. F. Hawley, Direct calculation of the radiative efficiency of an accretion disk around a black hole, *The Astrophysical Journal* **692**, 411 (2009).

[81] A. Murguia-Berthier, S. C. Noble, L. F. Roberts, E. Ramirez-Ruiz, L. R. Werneck, M. Kolacki, Z. B. Etienne, M. Avara, M. Campanelli, R. Ciolfi, F. Cipolletta, B. Drachler, L. Ennoggi, J. Faber, G. Fiacco, B. Giacomazzo, T. Gupte, T. Ha, B. J. Kelly, J. H. Krolik, F. G. L. Armengol, B. Margalit, T. Moon, R. O’Shaughnessy, J. M. Rueda-Becerril, J. Schnittman, Y. Zenati, and Y. Zlochower, HARM3D+NUC: A new method for simulating the post-merger phase of binary neutron star mergers with GRMHD, tabulated EOS, and neutrino leakage, *The Astrophysical Journal* **919**, 95 (2021).

[82] F. Cipolletta, J. V. Kalinani, B. Giacomazzo, and R. Ciolfi, Spritz: a new fully general-relativistic magnetohydrodynamic code, *Classical and Quantum Gravity* **37**, 135010 (2020).

[83] See <http://www.cactuscode.org/>.

[84] T. Goodale, G. Allen, G. Lanfermann, J. Massó, T. Radke, E. Seidel, and J. Shalf, The Cactus framework and toolkit: Design and applications, in *Vector and Parallel Processing – VECPAR’2002, 5th International Conference, Lecture Notes in Computer Science* (Springer, Berlin, 2003).

[85] E. Schnetter, S. H. Hawley, and I. Hawke, Evolutions in 3-D numerical relativity using fixed mesh refinement, *Class. Quantum Grav.* **21**, 1465 (2004).

[86] F. Löffler, J. Faber, E. Bentivegna, T. Bode, P. Diener, R. Haas, I. Hinder, B. C. Mundim, C. D. Ott, E. Schnetter, G. D. Allen, M. Campanelli, and P. Laguna, The Einstein Toolkit: A Community Computational Infrastructure for Relativistic Astrophysics, *Class. Quant. Grav.* **29**, 115001 (2012).

[87] R. Haas *et al.*, The einstein toolkit (2020), to find out more, visit <http://einstein toolkit.org>.

[88] P. Colella and P. R. Woodward, The piecewise parabolic method (ppm) for gas-dynamical simulations, *Journal of Computational Physics* **54**, 174 (1984).

[89] G. Toth, The  $\nabla \cdot B = 0$  constraint in shock-capturing magnetohydrodynamics codes, *Journal of Computational Physics* **161**, 605 (2000).

[90] C. R. Evans and J. F. Hawley, Simulation of Magnetohydrodynamic Flows: A Constrained Transport Model, *The Astrophysical Journal* **332**, 659 (1988).

[91] The definition of the magnetic field primitives in ILLINOISGRMHD differs from the definition introduced previously in this manuscript. Specifically  $B^k = B_{IGM}^k / (\alpha \sqrt{4\pi})$ .

[92] S. C. Noble, C. F. Gammie, J. C. McKinney, and L. D. Zanna, Primitive variable solvers for conservative general relativistic magnetohydrodynamics, *The Astrophysical Journal* **641**, 626 (2006).

[93] Z. B. Etienne, Y. T. Liu, V. Paschalidis, and S. L. Shapiro, General relativistic simulations of black hole-neutron star mergers: Effects of magnetic fields, *Phys. Rev. D* **85**, 064029 (2012).

[94] R. Arnowitt, S. Deser, and C. W. Misner, Chapter 7, in *Gravitation: An introduction to current research*, edited by L. Witten (Wiley, 1962) pp. 227–265.

[95] T. Nakamura, K. Oohara, and Y. Kojima, General Relativistic Collapse to Black Holes and Gravitational Waves from Black Holes, *Progress of Theoretical Physics Supplement* **90**, 1 (1987).

[96] M. Shibata and T. Nakamura, Evolution of three-dimensional gravitational waves: Harmonic slicing case, *Phys. Rev. D* **52**, 5428 (1995).

[97] T. W. Baumgarte and S. L. Shapiro, Numerical integration of einstein’s field equations, *Phys. Rev. D* **59**, 024007 (1998).

[98] See <https://www.cct.lsu.edu/~eschnett/McLachlan/>.

[99] J. D. Brown, P. Diener, O. Sarbach, E. Schnetter, and M. Tiglio, Turduckening black holes: an analytical and computational study, *Phys. Rev. D* **79**, 044023 (2009).

[100] See <http://kranccode.org/>.

[101] Publicly available at [https://github.com/zachetienne/nrpytutorial/blob/master/Tutorial-ETK\\_thorn-Interpolation\\_to\\_Arbitrary\\_Grids\\_multi\\_order.ipynb](https://github.com/zachetienne/nrpytutorial/blob/master/Tutorial-ETK_thorn-Interpolation_to_Arbitrary_Grids_multi_order.ipynb).

[102] M. Zilhão and S. C. Noble, Dynamic fisheye grids for binary black hole simulations, *Classical and Quantum Gravity* **31**, 065013 (2014).

[103] C. F. Gammie, J. C. McKinney, and G. Toth, HARM: A numerical scheme for general relativistic magnetohydrodynamics, *The Astrophysical Journal* **589**, 444 (2003).

[104] L. G. Fishbone and V. Moncrief, Relativistic fluid disks in orbit around Kerr black holes., *The Astrophysical Journal* **207**, 962 (1976).

[105] O. Porth *et al.*, The Event Horizon General Relativistic Magnetohydrodynamic Code Comparison Project, *Astrophysical Journal Supplement Series* **243**, 26 (2019).

[106] J. C. McKinney and C. F. Gammie, A measurement of the electromagnetic luminosity of a kerr black hole, *The Astrophysical Journal* **611**, 977 (2004).

[107] J. Thornburg, A Fast Apparent-Horizon Finder for 3-Dimensional Cartesian Grids in Numerical Relativity, *Class. Quantum Grav.* **21**, 743 (2004).

[108] S. C. Noble, B. C. Mundim, H. Nakano, J. H. Krolik, M. Campanelli, Y. Zlochower, and N. Yunes, Circumbinary Magnetohydrodynamic Accretion into Inspiring Binary Black Holes, *The Astrophysical Journal* **755**, 51 (2012).

[109] O. Dreyer, B. Krishnan, D. Shoemaker, and E. Schnetter, Introduction to isolated horizons in numerical relativity, *Phys. Rev. D* **67**, 024018 (2003).

[110] D. M. Siegel and B. D. Metzger, Three-dimensional

general-relativistic magnetohydrodynamic simulations of remnant accretion disks from neutron star mergers: Outflows and  $r$ -process nucleosynthesis, *Phys. Rev. Lett.* **119**, 231102 (2017).

[111] L. Franci, R. De Pietri, K. Dionysopoulou, and L. Rezzolla, Dynamical bar-mode instability in rotating and magnetized relativistic stars, *Phys. Rev. D* **88**, 104028 (2013).

[112] Y. Sekiguchi, K. Kiuchi, K. Kyutoku, and M. Shibata, Dynamical mass ejection from binary neutron star mergers: Radiation-hydrodynamics study in general relativity, *Phys. Rev. D* **91**, 064059 (2015).

[113] Visit <https://frontera-portal.tacc.utexas.edu/>.

[114] J.-P. De Villiers, J. F. Hawley, J. H. Krolik, and S. Hirase, Magnetically Driven Accretion in the Kerr Metric. III. Unbound Outflows, *The Astrophysical Journal* **620**, 878 (2005).

[115] K. Beckwith, J. F. Hawley, and J. H. Krolik, The Influence of Magnetic Field Geometry on the Evolution of Black Hole Accretion Flows: Similar Disks, Drastically Different Jets, *The Astrophysical Journal* **678**, 1180 (2008).

[116] J. C. McKinney, A. Tchekhovskoy, and R. D. Blandford, General relativistic magnetohydrodynamic simulations of magnetically choked accretion flows around black holes, *Monthly Notices of the Royal Astronomical Society* **423**, 3083 (2012).

[117] P. Mösta, D. Radice, R. Haas, E. Schnetter, and S. Bernuzzi, A magnetar engine for short GRBs and kilonovae, *The Astrophysical Journal* **901**, L37 (2020).

[118] K. A. Sorathia, C. S. Reynolds, J. M. Stone, and K. Beckwith, Global Simulations of Accretion Disks. I. Convergence and Comparisons with Local Models, *The Astrophysical Journal* **749**, 189 (2012).

[119] M. Nakamura, K. Asada, K. Hada, H.-Y. Pu, S. Noble, C. Tseng, K. Toma, M. Kino, H. Nagai, K. Takahashi, J.-C. Algaba, M. Orienti, K. Akiyama, A. Doi, G. Giovannini, M. Giroletti, M. Honma, S. Koyama, R. Lico, K. Niinuma, and F. Tazaki, Parabolic Jets from the Spinning Black Hole in M87, *The Astrophysical Journal* **868**, 146 (2018).

[120] D. B. Bowen, V. Mewes, S. C. Noble, M. Avara, M. Campanelli, and J. H. Krolik, Quasi-periodicity of supermassive binary black hole accretion approaching merger, *The Astrophysical Journal* **879**, 76 (2019).

[121] M. Liska, C. Hesp, A. Tchekhovskoy, A. Ingram, M. van der Klis, and S. Markoff, Formation of precessing jets by tilted black hole discs in 3D general relativistic MHD simulations, *Monthly Notices of the Royal Astronomical Society: Letters* **474**, L81 (2017).

[122] J. F. Hawley, X. Guan, and J. H. Krolik, Assessing quantitative results in accretion simulations: From local to global, *The Astrophysical Journal* **738**, 84 (2011).

[123] J. F. Hawley, S. A. Richers, X. Guan, and J. H. Krolik, Testing convergence for global accretion disks, *The Astrophysical Journal* **772**, 102 (2013).